Investigation of the Ignition of Fine Iron Particles in the Knudsen Transition Regime

Joel Jean-Philyppe, Faculty of Engineering

McGill University, Montreal

December 2021

A thesis submitted to McGill University in partial fulfillment of the requirements of the degree of:

Bachelor of Engineering, Honours Mechanical Engineering

Abstract

A computational model is considered to predict the ambient gas temperature at which fine iron particles can undergo thermal runaway and ignite. The model accounts for Knudsen transition transport effects, which become significant when the particle size becomes comparable to the mean free path of the gas molecules. The model considers the transient iron oxide layer growth at the surface of the iron particle in the kinetic formulation for iron oxidation. Values of the thermal accommodation coefficient for heat transport are computed using a calibrated semi-empirical correlation, while values of the sticking coefficient for mass transport are assumed. The ignition temperature as a function of particle size and initial oxide layer thickness is resolved using the transient computational model. In the free-molecular limit (small particles), the thermal insulating effect of the transition transport is shown to lead to a decrease in ignition temperature with decreasing particle size for a constant proportion of initial oxide layer thickness to total particle size (oxide layer thickness ratio). In the continuum limit (large particles), the ignition temperature is shown to be independent of particle size and is only a function of the oxide layer thickness ratio. The inhibiting effect of large initial oxide layers on the reaction kinetics is shown to lead to an asymptotic behavior of the ignition temperature as this ratio tends to 1, both in the free-molecular and continuum limits. Continuum transport modeling is shown to accurately predict ignition temperatures to within 5% error for particles exceeding 5 μm initial diameter, and to within 1% error for particles exceeding 40 μm. These results correspond to errors of 10-50 K on ignition temperatures neighboring $\approx$ 1000 K which are negligible. Continuum transport modeling is shown to be largely sufficient to model transport processes for particles in the tens or hundreds of microns.

Abrégé

Une formulation mathématique est élaborée pour prédire la température ambiante à laquelle une fine particule de fer peut s'enflammer. Le modèle tient compte de l'impact du régime de transition Knudsen sur le transfert de chaleur et de masse. Ces effets s'avèrent significatifs lorsque la taille des particules est comparable à la distance moyenne libre parcourue par les molécules de gas. Le modèle tient compte de la croissance d'une couche d'oxyde de fer à la surface de la particule. Le coefficient d'accommodation thermique est déduit d'une corrélation semi-empirique et le coefficient d'adsorption est assumé. La température d'inflammation en fonction de la taille des particules et de l'épaisseur initiale de la couche d'oxyde est résolue. Dans la limite où le transport moléculaire libre domine (petites particules), le transfert de chaleur réduit mène à une diminution de la température minimale d'inflammation avec une diminution de la taille des particules, pour un ratio constant entre l'épaisseur initiale de la couche d'oxyde et la taille de la particule. Dans la limite où les lois de transports macroscopiques dominent (larges particules), la température d'inflammation s'avère indépendante de la taille des particules et est uniquement une fonction du ratio de la couche d'oxyde. L'effet inhibiteur de larges couches d'oxyde sur la cinétique de l'oxydation du fer mène à un comportement asymptotique de la température d'inflammation lorsque ce ratio tend vers 1. Également, utiliser uniquement les lois macroscopiques mène à une erreur de moins de 5% pour des particules dépassant 5 μm, et à moins de 1% lorsqu'elles dépassent 40 μm. Ces erreurs correspondent à des différences de 10-50 K sur des températures d'inflammation d'environ 1000 K et sont négligeables. La modélisation par les lois macroscopiques est largement suffisante pour des particules de plusieurs dizaines ou centaines de micromètres.

Acknowledgements

I would like to express my special thanks and gratitude to my collaborator Dr. XiaoCheng Mi for his invaluable guidance and advice throughout the realization of this thesis, and for several insightful discussions on the key physics underlying the present work. I would also like to extend my special gratitude to Professor Jeffrey M. Bergthorson for his critical feedback in the completion of this thesis, and to colleague Aki Fujinawa for several discussions on the governing physics and on numerical implementation approaches.

Additionally, I would like to extend my gratitude to all the Metal Fuels group of the Alternative Fuels Laboratory of the Department of Mechanical Engineering of McGill University, supervised by Professor Jeffrey M. Bergthorson, for numerous insightful discussions, suggestions, and advice throughout the development of this work.

Table of Contents

List of Figures

List of Tables

Chapter 1

Introduction

Fossil fuels have dominated the energy industry over the past centuries due to their abundance, reliability, high energy density and specific energy, and ease of handling and storage. These characteristics position them as excellent energy-trading commodities and transportation fuels [4]. However, a pressing need to transition to zero-carbon, clean energy sources in our societies has arisen over the past decades. Indeed, human-driven combustion of fossil fuels is a prime contributor to accelerated climate change, which has negative impacts on human agricultural food production, the survival of terrestrial and marine ecosystems, the frequency and magnitude of natural disasters, the rising of sea levels, and several other aspects [5, 6]. Renewable energy sources such as hydroelectric, solar, and wind power constitute alternatives to fossil fuels for power generation. Although the cost of these sources has greatly decreased over the past decades, they present the disadvantage of being intermittent, and they cannot be stored directly. Furthermore, their relevance is strongly weather- and location- dependent. Consequently, alternative energy carriers which can substitute fossil fuels must be developed.

Over the past decades, several alternatives to fossil fuels were proposed, such as biofuels, batteries, hydrogen fuel cells, and advanced nuclear energy. In the recent years, metal fuels in the form of powders have increasingly received attention, due to their potential for creating a closed-loop, net zero-carbon energy commodity cycle [1]. Indeed, combustion of metal powders results in the

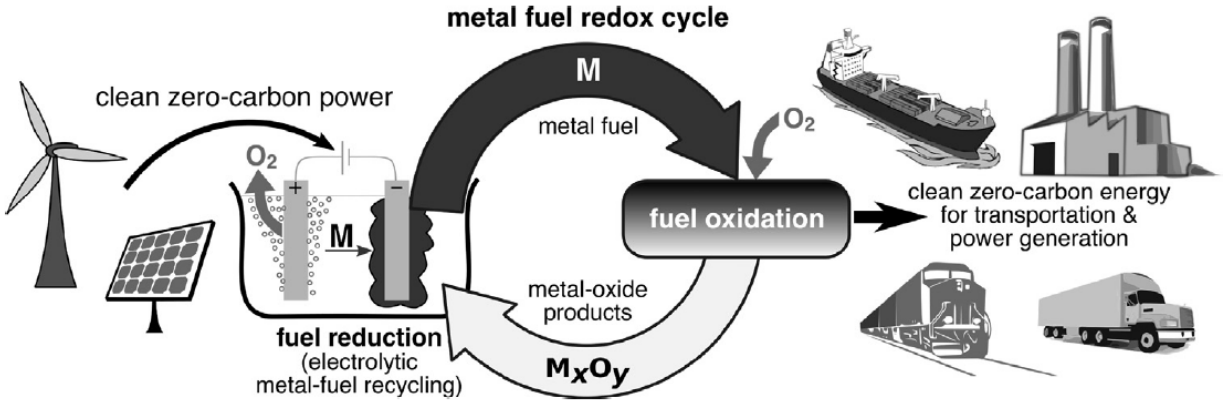

Figure 1.1: Closed-loop low-carbon metal fuel cycle. Taken from [1].

formation of metal oxides, harmless products that can be captured, reduced to their metallic form, and re-used as fuels, as illustrated in Figure 1.1. Amongst metals, iron has an excellent potential for global energy carriage and stationary power generation, due to its high energy density, its abundance, and the widely-developed iron mining, production, and recycling industries which currently exist [1].

A key technological barrier to the use of metals as energy carriers is the current lack of metal burners capable of producing usable power at scales relevant to the industrial sector. To optimize such systems, a challenge which persists is the development of a fundamental understanding of the key physics underlying metal combustion in the scientific community. Indeed, the mechanisms governing heterogeneous combustion between a solid fuel and a gaseous oxidizer were not as widely studied and developed as homogeneous, purely gaseous flames in the past decades, in the context of the rise of fossil fuels as global energy commodities. However, an understanding of these physics is essential in predicting and optimizing the performance of practical metal burners.

A concept arising in heterogeneous combustion is the ignition phenomenon of solid fuel particles [2, 7]. When ignited, particles transition to a burning regime exhibiting rapid reaction kinetics and high energy release rates. Metal burners with ignited particles therefore present the potential for practical, high-power energy applications, which motivates the need to accurately predict the ignition behavior of such particles. Amongst condensed-phase fuels, metals are typically set apart

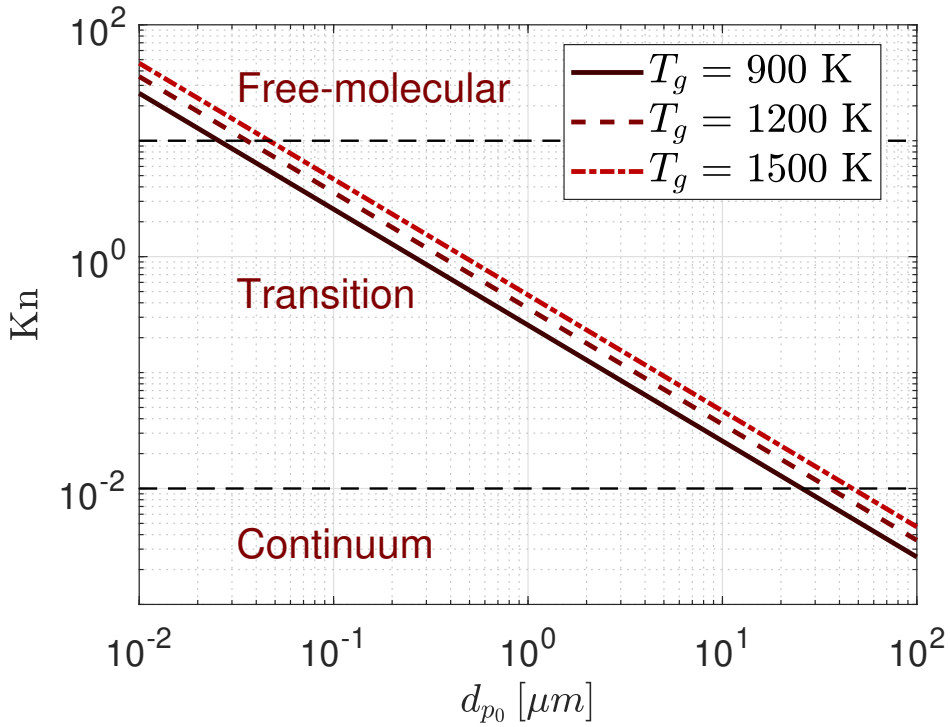

Figure 1.2: Knudsen number and transport regimes as a function of particle size for a 21%-79% O_2-N_2 gas mixture, at 1 atm pressure and different gas temperatures T_g. For T_g = 1500 K, the transition and free-molecular regimes respectively onset for particles below $\approx$ 47 μm and 47 nm.

by the formation of an oxide layer at their surface, which shields them from the oxidizer gas and hinders the particle ignition process [8,9]. Literature on the oxidation and ignition behavior of metals was developed in the past decades [8–12], and a computational model for iron-specific ignition considering the growth of the oxide scale at its surface was recently proposed [3]. Conventionally, the continuum assumption has been adopted to describe heat and mass transport in metal combustion problems. However, this assumption fails to accurately predict transport processes when the solid particles are of comparable size or smaller than the mean free path of the gas molecules. This is quantified by the Knudsen number, which is the ratio of the molecular mean free path to the particle radius. It is generally accepted that at Knudsen numbers less than 0.01, continuum treatment accurately describes the transport processes, while at Knudsen numbers larger than 10, free-molecular transport governs [13–16]. At intermediate Knudsen numbers, transport processes are described by the transition regime. These concepts are illustrated in Figure 1.2.

In applications pertaining to heterogeneous reactions, authors typically reported transition effects must imperatively be considered for relatively small particles. In aerosol particle reaction problems, Gopalakrishnan et al. [13] reported transition effects must be considered for submicrometer and nanoparticles at atmospheric pressures. Shpara et al. [16] considered the combustion of boron particles with air and established the onset of transition effects between 1.23 μm and 46.3 μm for pressures ranging from 0.10 to 4.0 MPa, with adiabatic flame temperatures around 2900 K. Mohan et al. [17] considered the heating and ignition delay time of metallic particles placed in a hot gas and established the onset of transition effects at 18 μm and 2 μm for pressures of 1 bar and 10 bars, respectively. Controversially, Senyurt & Dreizin [18] recently studied the ignition of aluminum, boron, and magnesium particles at atmospheric pressure, and stated that transition effects must be considered for particles of up to 200 μm. This controversy motivates further investigation of this problem; as well, Knudsen transition effects were not previously considered in iron-specific combustion problems.

The current work aims to advance the knowledge of the physics underlying metal combustion, specifically by conducting a quantitative computational study of the ignition behavior of fine iron particles across the Knudsen transition regime. The model proposed considers iron-specific oxidation kinetics, with transient solid iron oxide layer growth. Transition transport phenomena are incorporated through a flux-matching boundary sphere approach. This study attempts to answer the following scientific questions:

- What is the impact of transition transport on the ignition behavior of isolated iron particles?
- At what minimum particle size can continuum transport be considered to accurately model and predict the ignition behavior of such particles at atmospheric pressure?

To approach these questions, a brief theoretical background of the key physics underlying heterogeneous combustion mechanisms, solid-phase iron oxidation, and heat and mass transport is provided in Chapters 2 and 3. A computational model incorporating these physics is then detailed in Chapter 4, and key results, discussions, and conclusions are presented in Chapter 5.

Chapter 2

Combustion of an Isolated Particle

The foundational theory on heterogeneous reactions was developed by Frank-Kamenetskii [7] based on the method of the uniformly accessible surface. In his work, Frank-Kamenetskii extended the established theory of homogeneous gas-phase reactions to describe combustion mechanisms of a solid fuel with a gaseous oxidizer. Based on this theory, Soo et al. [2] developped a detailed analysis of the ignition characteristics of metallic particles, suspensions of particles, and agglomerates. Mi et al. [3] specialized this analysis to describe the ignition behavior of fine iron particles. The development of these different theories is summarized in the current chapter, in the context of reaction mechanisms of an isolated particle.

2.1 Heterogeneous Combustion Mechanisms

The method of the uniformly accessible surface developed by Frank-Kamenetskii [7] postulates a quasi-steady state or quasi-stationary assumption on heterogeneous reactions: the concentration of oxidizer at the particle surface and in the diffusion boundary layer instantaneously adjusts to the consumption rate of oxidizer by the particle, as shown in Figure 2.1. This led to the development of an effective reaction rate, which incorporates the interplay between the kinetic consumption rate and the diffusion transport rate of the oxidizer. The current section details these concepts.

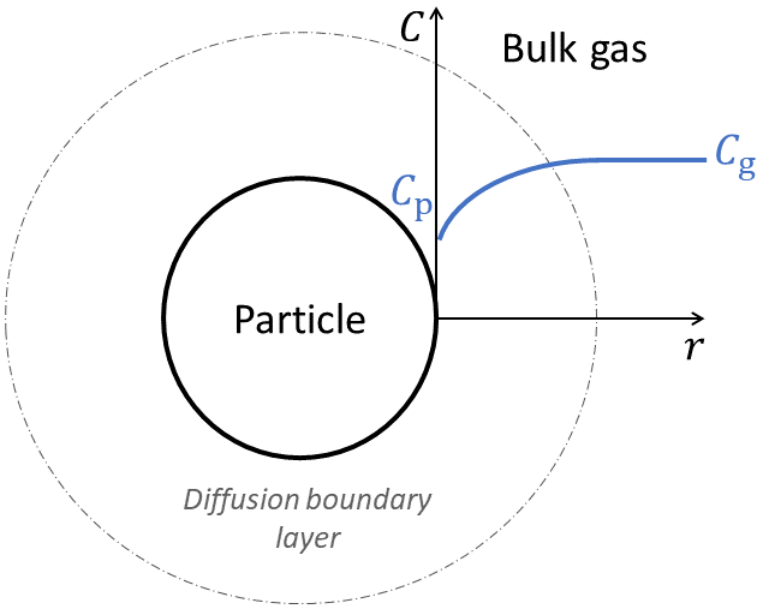

Figure 2.1: Oxidizer concentration profile around a reacting particle in an oxidizing gas.

2.1.1 The $k - \beta$ Effective Reaction Rate

Assuming the continuum regime describes transport processes, the diffusion rate of oxidizer from the bulk gas to the particle surface is formulated as:

$$j = \beta(C_{\mathrm{g}} - C_{\mathrm{p}}) \tag{2.1}$$

where j is the diffusive flux, β is the diffusive velocity, C_{g} is the concentration of oxidizer in the bulk gas, and C_{p} is the concentration at the particle surface. For a spherical particle, the theory of similitude permits the development of the following expression for the diffusive velocity [7]:

$$\beta = \frac{\mathrm{Nu}D}{2r_{\mathrm{p}}} \tag{2.2}$$

where Nu is the Nusselt number, D is the diffusion coefficient of the oxidizer in the gas mixture, and r_{p} is the particle radius. Over the past decades, experimental data allowed to develop semi-empirical Nusselt number correlations for different flow conditions and geometric configurations;

those are readily available in the litterature [19, 20]. For a spherical particle in a stationary gas, the well-known result Nu = 2 can be obtained from theoretical considerations only [19].

Frank-Kamenetskii formulates the regression rate of the fuel particle as a function of the oxidizer concentration at the particle surface, $\dot{\omega} = f(C_{\mathrm{p}})$ [7]. Assuming the simplest case, where the surface reaction is governed by first-order kinetics, the formulation

$$\dot{\omega} = kC_{\mathrm{p}} \tag{2.3}$$

is obtained, where $k = k_0 \exp\left(-T_{\mathrm{a}}/T_{\mathrm{p}}\right)$ is the kinetic rate expressed in an Arrhenius form, with k_0 the Arrhenius constant, T_{a} the activation temperature, and T_{p} the particle temperature [2, 7]. By the quasi-stationary postulate, the diffusive flux towards the particle surface can be equated to the consumption rate of oxidizer at the particle surface, $\beta(C_{\mathrm{g}} - C_{\mathrm{p}}) = kC_{\mathrm{p}}$. Solving for the oxidizer concentration at the particle surface:

$$C_{\mathrm{p}} = \frac{\beta C_{\mathrm{g}}}{k + \beta} \tag{2.4}$$

and substituting in Equation 2.3:

$$\dot{\omega} = \frac{k\beta}{k + \beta} C_{\mathrm{g}} \equiv k_{\mathrm{eff}} C_{\mathrm{g}} \tag{2.5}$$

where k_{eff} is an effective reaction rate. The effective reaction rate incorporates the interaction between the kinetic surface consumption rate of oxidizer and the diffusive rate of oxidizer from the bulk gas to the particle. This interaction can be referred to as the generic $k - \beta$ formulation for first-order heterogeneous reactions.

2.1.2 Particle Ignition and Thermal Regimes of Reaction

The theory of thermal ignition developed by Semenov for homogeneous reactions can be extended to heterogeneous reactions to describe the thermal regimes of burning particles [2, 7]. In this analysis, it is assumed that the oxidizing gas mixture is in sufficient quantity such that the combustion of an isolated particle does not influence the properties of the bulk gas. Following Soo [2], the heat

generated by a reacting particle can be formulated as $\dot{Q}_{\mathrm{R}} = q\nu A_{\mathrm{p}} k_{\mathrm{eff}} C_{\mathrm{g}}$, where q is the gravimetric heating value of the fuel, ν is the stoichiometric coefficient relating the mass of fuel consumed per mass of oxidizer, and A_{p} is the particle surface area. The conductive heat loss rate from the particle to the gas in the continuum regime is described by $\dot{Q}_{\mathrm{L}} = 4\pi r_{\mathrm{p}} k_{\mathrm{g}} (T_{\mathrm{p}} - T_{\mathrm{g}}) \equiv h A_{\mathrm{p}} (T_{\mathrm{p}} - T_{\mathrm{g}})$, where $h = k_{\mathrm{g}}/r_{\mathrm{p}}$ is the convective heat transfer coefficient. Thermal explosion of the particle occurs when the heat generation rate exceeds the heat loss rate, $q\nu A_{\mathrm{p}} k_{\mathrm{eff}} C_{\mathrm{g}} > h A_{\mathrm{p}} (T_{\mathrm{p}} - T_{\mathrm{g}})$. Expanding this criterion yields:

$$q\nu \left(\frac{k\beta}{k+\beta} \right) C_{\mathrm{g}} > \frac{k_{\mathrm{g}}}{r_{\mathrm{p}}} (T_{\mathrm{p}} - T_{\mathrm{g}}). \tag{2.6}$$

Substituting the diffusive velocity in the numerator by Equation 2.2 and using $\mathrm{Nu} = 2$ for a spherical particle in a stationary gas results in:

$$\left(\frac{k}{k+\beta} \right) q\nu D C_{\mathrm{g}} > k_{\mathrm{g}} (T_{\mathrm{p}} - T_{\mathrm{g}}). \tag{2.7}$$

If the diffusive rate of oxidizer is much faster than the kinetic consumption rate at the particle surface, then $\beta >> k$ and the particle is said to burn in the kinetic-limited regime. Taking the limit $\beta >> k$ of Equation 2.7 yields $0 > k_{\mathrm{g}} (T_{\mathrm{p}} - T_{\mathrm{g}})$, which obviously is an impossible result. Hence in the kinetic-limited regime, the particle cannot ignite, and its burning temperature will remain close to the bulk gas temperature, hence $T_{\mathrm{p}} \rightarrow T_{\mathrm{g}}$. Conversely, if the diffusive rate of oxidizer is much slower than the kinetic consumption rate at the particle surface, then $k >> \beta$ and the particle is said to burn in the diffusive-limited regime. Taking the limit $k >> \beta$ in Equation 2.7 yields $q\nu D C_{\mathrm{g}} > k_{\mathrm{g}} (T_{\mathrm{p}} - T_{\mathrm{g}})$, which constitutes the ignition criterion. The particle temperature will then tend towards:

$$T_{\mathrm{p}} \rightarrow T_{\mathrm{g}} + \frac{q\nu D C_{\mathrm{g}}}{k_{\mathrm{g}}}. \tag{2.8}$$

Using the thermal diffusivity $\alpha = k_{\mathrm{g}}/(\rho c_p)$, where ρ is the gas density and c_p is its heat capacity, Equation 2.8 can be re-written as:

$$T_{\mathrm{p}} \rightarrow T_{\mathrm{g}} + \frac{D}{\alpha} \frac{q\nu C_{\mathrm{g}}}{\rho c_p}. \tag{2.9}$$

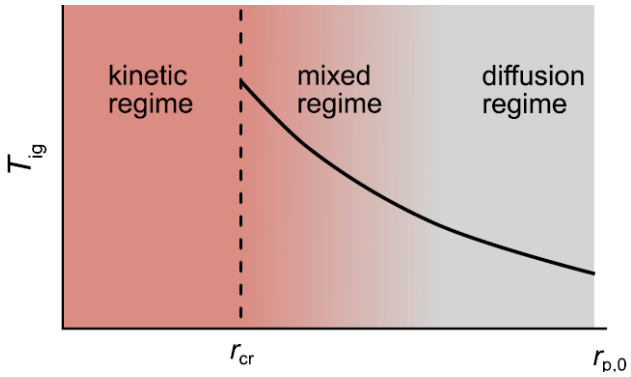

Figure 2.2: Qualitative behavior of the bulk gas temperature $T_g = T_{ig}$ leading to particle ignition as a function of initial particle radius $r_{p,0}$. Below a critical particle size r_{cr}, the particle cannot ignite. Taken from [2].

In the case of a unity Lewis number, Le $= \alpha/D \equiv 1$, this results in:

$$T_p \rightarrow T_g + \frac{q\nu C_g}{\rho c_p} = T_{stoich} \tag{2.10}$$

where T_{stoich} is the maximum possible particle burning temperature. It is equal to the flame temperature of a particle-gas mixture, assuming the reaction products negligibly contribute to the overall heat capacity of the mixture [2, 7]. Heterogeneous reactions are therefore characterized by the ability of particles to ignite and burn above the gas temperature, close to the stoichiometric flame temperature. This ignition phenomenon occurs in the diffusive-limited combustion regime, and it is naturally captured by the interplay between the kinetic and diffusive consumption rates of oxidizer as formulated by the $k - \beta$ effective reaction rate.

Vulis [21] showed analytically that the ignition temperature of a particle can be obtained by satisfying the Semenov criteria, wherein $\dot{Q}_R = \dot{Q}_L$ and $d\dot{Q}_R/dT_p = d\dot{Q}_L/dT_p$. If continuum transport predominates across the range of particle sizes considered, the ignition criteria degenerate as the particle size is being decreased, and the apparition of a minimum critical size for particle ignition is observed, as shown in Figure 2.2 [2]. Below this critical particle size, the ratio of the surface area exposed to continuum conductive heat loss relative to the volumetric heat generation rate of

the particle becomes sufficiently large such that the Semenov ignition criteria cannot be satisfied for any real gas temperature.

2.2 Solid-Phase Iron Oxidation

The generic $k - \beta$ formulation captures the interplay between diffusive- and kinetic- limited combustion for heterogeneous reactions governed by fist-order kinetics. This formulation only considers the oxidizer concentration at the particle surface and the particle temperature, as described by Equation 2.3. In reality, a majority of metals accumulate metal oxides at their surface as they oxidize, and the oxygen must diffuse through these oxide layers to react with the metal fuel. If the diffusion rate of the ions through the oxide layers is much slower than the reaction rate of the ions at the interfaces to produce metal oxides, then the accumulated oxide layers at the particle surface inhibit the global reaction kinetics of the particle. This was experimentally demonstrated to be the case for iron oxidation in the temperature interval 973 K to 1523 K by Païdassi [22]. Based on Païdassi's experimental results, Mi et al. [3] proposed a kinetic model for iron oxidation considering the growth of oxide layers on the particle. The current section summarizes the key concepts underlying this formulation.

2.2.1 Underlying Physics

Païdassi [22] conducted experiments in the 1950s to characterize the solid-phase oxidation behavior of iron films. He demonstrated that isothermal solid-phase iron oxidation in the temperature range 973 K to 1523 K always results in the formation of three compact iron oxide layers on the iron surface. From the outermost layer to the innermost layer, the oxides formed are Fe_2O_3 (hematite), Fe_3O_4 (magnetite), and FeO (wüstite). The proportion of each oxide layer thickness to the total thickness of the oxide scale was reported to be 95% FeO, 4% Fe_3O_4, and 1% Fe_2O_3. These proportions remained constant for all isothermal oxidation curves. The multi-layered oxidation process of iron is illustrated in Figure 2.3 and can be summarized as follows [3]:

1. Diffusion of O_2 from the bulk gas to the gas-oxide interface.

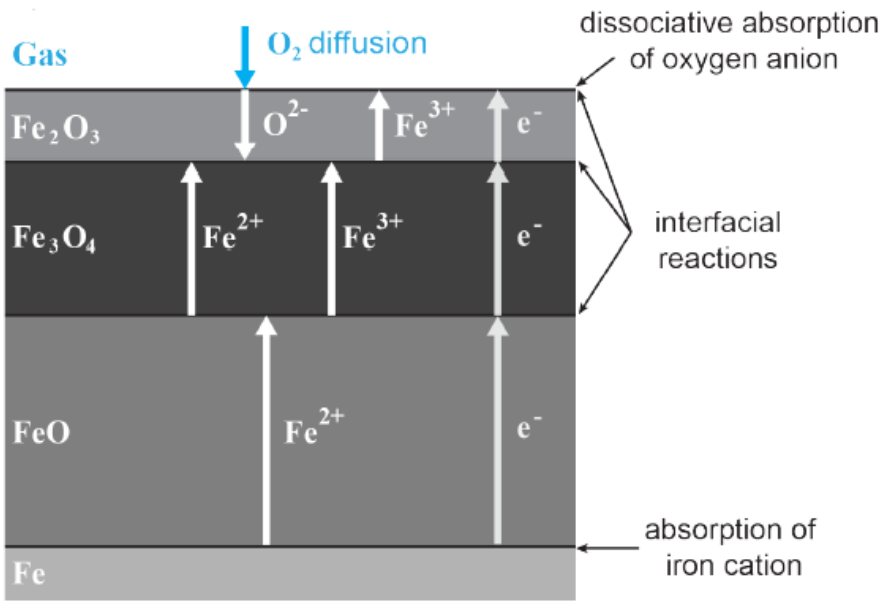

Figure 2.3: Schematic of the key processes underlying solid-phase iron oxidation. Taken from [3].

2. Incorporation of anions O^{2-} into the oxide scale.

3. Absorption of cations Fe^{2+} into the oxide scale.

4. Diffusion of ions and electrons through the oxide scale.

5. Reaction at FeO-Fe_3O_4, Fe_3O_4-Fe_2O_3, and Fe_2O_3-O_2 interfaces.

In his work, Païdassi obtained experimental curves for the growth rate of the different iron oxide layers at isothermal conditions. He revealed that the thickness of the oxide layers X_i increases with the square root of time $\sqrt{t}$ at a constant rate k_i, following a parabolic rate law. This is formulated as $X_i = k_i\sqrt{t} + X_{i,0}$, where $X_{i,0}$ is the initial oxide layer thickness. The kinetic constant k_i is a function of temperature. The parabolic growth rate of the oxide layers implies that the oxidation process is controlled by the diffusion rate of ions inside the oxide films [22]. In fact, the reaction rates of the ions at the interfaces significantly exceed the diffusion rates of ions, resulting in the latter process controlling the overall internal reaction kinetics.

Another key feature of iron oxidation demonstrated by Goursat & Smeltzer [23] is the independence of iron oxides growth rates on the surrounding oxidizer concentration at least in the interval 1073 K to 1273 K for a resulting partial pressure of oxygen exceeding 4 x 10^{-4} atm. This behavior originates from the external Fe_2O_3 layer at the particle surface, which adapts to the ambient oxidizer concentration and permits an independence of the internal kinetics of the particles at the inter-facial reactions [3].

2.2.2 Parabolic Kinetic Model

Based on Païdassi's experimental results, Mi et al. [3] formulated a kinetic model for solid-phase oxidation of a spherical iron particle consisting of a core of Fe, an inner layer of FeO, and an outer layer of Fe_3O_4. The thickness of Fe_2O_3 being only 1% of the total thickness of oxides, it contributes negligibly to heat release in the particle and is therefore not considered in the analysis. The kinetic growth rates of iron oxides reported by Païdassi [22] were converted to rate constants $k_{\mathrm{p},i}$ using: $k_{\mathrm{p},i} = \frac{k_i^2}{2}$, which allowed to write first order Arrhenius kinetics of the form:

$$k_{\mathrm{p},i} = k_{0,i} \exp\left(\frac{-T_{\mathrm{a},i}}{T_{\mathrm{p}}}\right). \tag{2.11}$$

Mi et al. [3] calibrated the rate constants based on Païdassi's experimental data [22]; results are provided in Section 4.5. The growth rate of the oxide layers can then be formulated as [3]:

$$\frac{dX_i}{dt} = \frac{k_{0,i}}{X_i} \exp\left(\frac{-T_{\mathrm{a},i}}{T_{\mathrm{p}}}\right). \tag{2.12}$$

It is of importance to note that the kinetic rates are independent of the oxidizer concentration at the particle surface. Nevertheless, the particle still possesses the ability to ignite and burn in the diffusive-limited combustion regime, as described in Section 2.1.2. The interplay between the kinetic and diffusive rates as captured by the $k-\beta$ formulation is specialized to iron by implementing a switch-type model for the consumption rate of oxidizer by the particle. Assuming the transport processes occur in the continuum regime, the maximum possible diffusion flux of oxidizer O_2 from

the bulk gas to the particle surface is obtained by setting $C_{\mathrm{p}} = 0$ in Equation 2.1:

$$j = \beta C_{\mathrm{g}} \equiv \left(\frac{D_{\mathrm{O_2}}}{r_{\mathrm{p}}} \right) C_{\mathrm{g}} \tag{2.13}$$

where $D_{\mathrm{O_2}}$ is the diffusion coefficient of O_2 in the gas mixture. Multiplying by the surface area of the particle, the maximum possible consumption rate of oxidizer by the particle is:

$$\dot{m}_{\mathrm{O_2}} = 4\pi r_{\mathrm{p}} D_{\mathrm{O_2}} C_{\mathrm{g}}. \tag{2.14}$$

The interplay between kinetic- and diffusive- limited combustion can be captured by comparing the rate of oxidizer consumption predicted by the maximum possible diffusion rate of oxidizer, to the rate of oxidizer consumption resulting from the parabolic kinetic reaction rate of the particle. The lowest value determines the combustion regime of the particle.

Chapter 3

Gas-Particle Heat and Mass Transfer

In applications related to heat and mass transfer between a gas and a particle such as solid-phase oxidation, the classical macroscopic laws of heat conduction and mass diffusion - Fourier's law and Fick's law - can fail to accurately predict these transport mechanisms. This failure is encountered when the mean free path of the gas molecules becomes comparable or much larger than the particle size. Instead, the appropriate approach arises from molecular gas kinetics theory, which considers the individual motion of gas molecules, the inter-molecular collision rate, and the molecule-particle collision rate. The non-dimensional Knudsen number allows to predict in which regime the molecular transport occurs: free-molecular, continuum, or transition regime. It is defined as the ratio of the mean free path of the gas molecules to the particle radius. The kinetic theory of gases provides solutions to heat and mass transport across the entire range of Knudsen number. This chapter provides an overview of these solutions. Analytical expressions and numerical methods are presented to model transport processes in the different regimes. This chapter only pertains to conductive heat transfer: radiation is not considered.

3.1 Molecular Mean Free Path

The molecular mean free path is essential in quantifying transport processes in gases. It constitutes the average distance traveled by gas molecules between inter-molecular collisions. The exact mathematical formulation of the mean free path depends on the molecular model used. In a Maxwellian gas, or a gas which has a velocity field described by the Maxwell-Boltzmann velocity distribution function at steady-state, the Maxwell mean free path for the hard elastic spheres molecular model is formulated as [24–26]:

$$\lambda_{\text{MFP}} = \frac{1}{\sqrt{2}\pi n \sigma^2} \tag{3.1}$$

where n is the number density of gas molecules and σ is the molecular diameter. Equation 3.1 presents a difficulty as it requires knowledge of the molecular diameter σ which may be difficult to estimate. Alternatively, the mean free path can be formulated from the gas viscosity μ, its density ρ, and its average thermal molecular speed $\bar{c}$ [24, 25] :

$$\lambda_{\text{MFP}} = \frac{2\mu}{\rho \bar{c}}. \tag{3.2}$$

Following Eucken, an accurate approximation for the hard spheres model is to relate the thermal conductivity k_{g}, heat capacity at constant volume c_v, and viscosity μ by the Eucken factor $f = \frac{1}{4}(9\gamma - 5)$, where γ is the heat capacity ratio. Then, $k_{\text{g}} = f\mu c_v$ [24, 25]. Using $c_p = c_v + R_{\text{g}}$, where c_p is the heat capacity at constant pressure and R_{g} is the individual gas constant; the Maxwellian mean molecular velocity $\bar{c} = \sqrt{8k_{\text{B}}T/(\pi m)}$, where k_{B} is the Boltzmann constant, T is gas temperature, and m is the individual molecular mass [25]; and the ideal gas law, Equation 3.2 can be re-written as:

$$\lambda_{\text{MFP}} = \frac{k_{\text{g}}(\gamma - 1)}{fp}\sqrt{\frac{\pi m T}{2k_{\text{B}}}}. \tag{3.3}$$

This formulation of the Maxwell mean free path is applicable to monoatomic and polyatomic gases under the hard elastic spheres molecular model [15].

3.2 Knudsen Number and Transport Regimes

Heat and mass transport in gases can be classified by different transport regimes as a function of the non dimensional Knudsen number Kn. It is defined as the ratio of the mean free path of the gas molecules to the characteristic length of the system L_c [14, 15]:

$$\mathrm{Kn} = \frac{\lambda_{\mathrm{MFP}}}{L_c}. \tag{3.4}$$

For transport phenomena between a spherical particle and a gas, the length scale can arbitrarily be defined as the particle diameter or radius. In the current work, the particle radius r_p is used. Three ranges of transport regimes can be identified, as schematically illustrated in Figure 3.1.

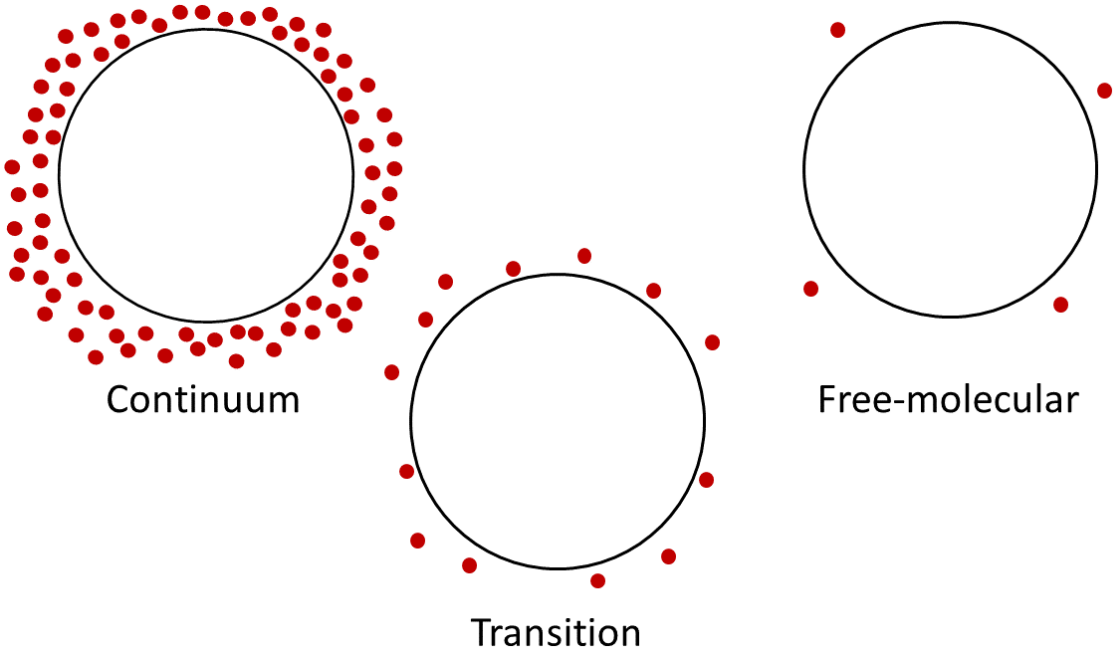

Figure 3.1: Schematic of the different transport regimes. Continuum: high inter-molecular and molecule-particle collision rates. Free-molecular: low collision rates. Transition: intermediate.

3.2.1 Free-Molecular Regime

For sufficiently large Knudsen number ($\mathrm{Kn} > 10$), transport processes occur purely in the free-molecular regime [13–16]. Equivalently, this regime is referred to as rarefied gas or low-pressure

regime. Equation 3.3 shows that λ_{MFP} is inversely proportional to gas pressure, giving rise to these appellations. Free-molecular transport is characterized by a large average traveling distance of the molecules between inter-molecular collisions, which are ballistic. As well, the small particle radius with respect to the mean free path implies a low molecule-particle collision rate. These concepts are illustrated in Figure 3.1. This low collision rate constitutes the limiting step for heat transfer, and it controls mass transfer in diffusive-limited heterogeneous combustion (Section 2.1.2).

When oxidizing gas molecules collide with a reactive particle surface, they are either reflected to the bulk gas or stick to the surface [14]. The fraction of impinging particles α_{M} that stick to it is equivalently referred to as trapping coefficient, sticking coefficient, or mass accommodation coefficient. The trapped oxidizer molecules can then be adsorbed and react with the fuel. In the diffusive-limited combustion regime, the collision rate multiplied by the sticking coefficient determines the reaction rate of the particle [14]. The sticking coefficient is typically a strong function of temperature and oxidizer coverage at the particle surface, until the surface of the particle is saturated, at which point α_{M} remains approximately constant [14, 27–31].

In the free-molecular regime, the mass flux of molecules crossing a unit surface area in one direction is [25]: $\Gamma_m = \frac{1}{4}\rho\bar{c}$, where ρ is the gas density. In a non-uniform gas, the net mass flux per unit surface area from location 1 to location 2 is therefore:

$$j_{\text{FM}} = \frac{1}{4}(\rho_1\bar{c}_1 - \rho_2\bar{c}_2). \tag{3.5}$$

Considering location 1 to be the bulk gas and location 2 to be the surface of the particle, and factoring in the surface area of the particle and the sticking probability of the colliding gas molecules, the mass consumption rate of oxidizer $\dot{m}_{\text{FM}}$ in the free-molecular regime is then described by:

$$\dot{m}_{\text{FM}} = \alpha_{\text{M}}\pi r_{\text{p}}^2(\rho_{\text{g}}\bar{c}_{\text{g}} - \rho_{\text{p}}\bar{c}_{\text{p}}) \tag{3.6}$$

where ρ is oxidizing gas density and the subscripts p and g respectively denote at the particle surface and in the bulk gas.

Analogous to mass transport, heat transfer in the free-molecular regime is governed by the molecule-particle collision rate. When gas molecules collide with the particle surface, a fraction of them slip without energy exchange. The proportion of collisions α_{T} resulting in effective heat transfer is referred to as the thermal accommodation coefficient or energy accommodation coefficient [25, 32]. The formal definition of the thermal accommodation coefficient is attributed to Knudsen and yields [25]:

$$\alpha_{\mathrm{T}} = \frac{(E_{\mathrm{o}} - E_{\mathrm{i}})}{(E_{\mathrm{o}} - E_{\mathrm{i}})_{\mathrm{max}}} \tag{3.7}$$

where E_{i} and E_{o} are respectively the energy of the incident and scattered molecules. The energy expressions in Equation 3.7 can equivalently be replaced by temperatures. The thermal accommodation coefficient is an extremely strong function of surface conditions. A dominant parameter is the solid surface composition, namely the adsorbed gas layers covering the solid, which contribute to energy exchange [25, 32–35]. The adsorbed layers can be related to the surface temperature for a specific solid-gas combination. A weaker dependency with gas pressure can also be established. Another key variable is the surface roughness, which impacts the number of collisions at each encounter between the gas molecules and the surface [25, 32, 33, 35]. Several classical theories for estimating accommodation coefficients were developed in the literature, yet there remains high uncertainty in the exact quantification of this parameter for specific surface conditions and solid-gas combinations. An important contribution was presented by Song & Yovanovich [33], who proposed a generic semi-empirical correlation for any solid-gas combination to be used in conjunction with experimental data.

Assuming the translational, rotational, and vibrational energy modes have equal accommodation coefficients, heat conduction between a gas and a spherical particle can be described by [15]:

$$\dot{Q}_{\mathrm{FM}} = \alpha_{\mathrm{T}} \pi r_{\mathrm{p}}^2 \frac{p\bar{c}}{2} \left(\frac{\gamma + 1}{\gamma - 1} \right) \left(\frac{T_{\mathrm{p}}}{T_{\mathrm{g}}} - 1 \right). \tag{3.8}$$

3.2.2 Continuum Regime

For sufficiently small Knudsen number (Kn < 0.01), heat and mass transfer occur in the continuum regime [13–16], equivalently referred to as the high pressure regime. It is characterized by high inter-molecular and molecule-particle collision rates, as illustrated in Figure 3.1. In this regime, the limiting step for heat transfer is the inability of the molecules colliding with the particle surface to effectively carry the energy away from the particle to the bulk gas before experiencing several collisions [15]. As well, a concentration gradient is established towards the particle surface, as shown in Figure 2.1, and mass transport occurs through the diffusion of oxidizer towards the particle surface.

In the continuum regime, Fick's law of diffusion describes the mass flux rate. For a reactive spherical particle exchanging mass with the surrounding gas, the oxidizer consumption rate is [36]:

$$\dot{m}_{\mathrm{C}} = 4\pi r_{\mathrm{p}} D (C_{\mathrm{g}} - C_{\mathrm{p}}) \tag{3.9}$$

where D is the oxidizer mass diffusivity in the gas mixture. Rigorous theory of transport phenomena allows to theoretically formulate the diffusion coefficient D from gas kinetics theory [24, 25, 37, 38]. Conjointly, several semi-empirical correlations were developed over the past decades to predict diffusion coefficients and provide good estimates under different circumstances. A number of them are reported by Green & Perry [39].

Analogous to mass transport, Fourier's law of heat conduction describes the heat transfer rate from a particle to a gas in the continuum regime [15]:

$$\dot{Q}_{\mathrm{C}} = 4\pi r_{\mathrm{p}} k_{\mathrm{g}} (T_{\mathrm{p}} - T_{\mathrm{g}}). \tag{3.10}$$

Correlations of species thermal conductivity are readily available in the literature [40].

3.2.3 Transition Regime

For intermediate Knudsen number ($0.01 \leq \text{Kn} \leq 10$), heat and mass transfer occur in the transition regime [13–16], where the gas molecular mean free path is comparable to the particle radius, and the transport mechanisms possess characteristics of both the continuum and the free-molecular limits. Conceptually speaking, the transition regime can be understood by delimiting two distinct regions around the particle surface where the transport rates are governed by different mechanisms. In the vicinity of the particle, there exists a collision-less region called the Knudsen layer or the Langmuir layer. Its thickness is in the order of the molecular mean free path, and transport mechanisms are governed by free-molecular gas kinetics in this region. Beyond the Knudsen layer, the transport mechanisms occur in continuum, where the macroscopic heat conduction and mass diffusion laws apply [14, 15].

The existence of the Knudsen boundary layer arising from molecular transport at the interface between two dissimilar phases gives rise to a jump in the temperature and oxidizer concentration of the bulk gas in the vicinity of the particle, causing a deviation from the profiles predicted by continuum [15, 25, 36, 38, 41], as shown in Figure 3.2. These temperature and concentration jumps were perhaps first observed experimentally by Smoluchowski [25, 42] and Bradley et al. [43], respectively. The jumps begin at the surface of the Knudsen layer, where the gradients of temperature and oxidizer concentration respectively rise and decrease sharply.

The Knudsen layer also exists in the continuum and the free-molecular limits. However, its small size relative to the particle in the former limit leads to a negligible impact of the gas kinetics transport effects at the particle surface, permitting solutions described purely by the macroscopic transport equations. Conversely, its large size relative to the particle in the latter limit implies that continuum transport beyond the Knudsen layer need not be considered.

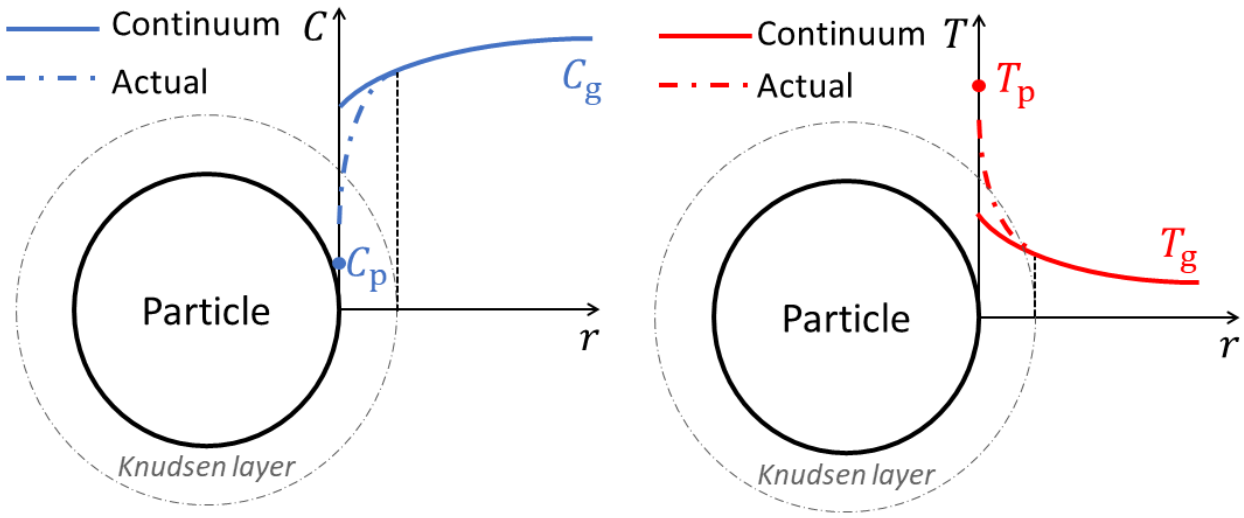

Figure 3.2: Temperature and concentration jump in the Knudsen layer. The profiles differ from the continuum solutions from the particle surface to the Knudsen layer boundary.

3.3 Modeling the Transition Regime

The transition regime presents an additional difficulty as there exists no analytical closed-form solution to describe the transport mechanisms in this range of Knudsen number. The heat and mass transfer are governed by the full Boltzmann equation, an integral-differential equation with initial and boundary conditions [14, 15]. Consequently, multiple modeling approaches to describe the transition regime were developed over the past decades. An elaborate review of transition heat conduction modeling employed in the laser-induced incandescence literature is presented by Liu et al. [15], whereas several methods for heat and mass transport prediction in droplet evaporation problems are reported by Wagner [38]. A number of these methods rely on applying a corrective transitional factor to the continuum transport rates based on the value of the Knudsen number. Other methods introduce a boundary sphere of thickness θ delimiting free-molecular and continuum transport regions, while the fluxes are matched in quasi-equilibrium. The following subsections report a specific method pertaining to these approaches.

3.3.1 Implicit Solution - Boundary Sphere Method

The perhaps most sophisticated approach to transition transport modeling and that which best approximates the physics involved is the boundary sphere flux-matching method. The earliest researchers to apply this method were Langmuir in problems considering conduction heat transfer from a wire [44], and Fuchs in droplet evaporation problems [36]. In the boundary sphere approach, a Knudsen layer of thickness θ closely related to the mean free path of the gas molecules is introduced in the vicinity of the particle. Transport mechanisms are assumed to occur in the free-molecular regime inside the Knudsen layer, and in the continuum regime beyond, as shown in Figure 3.3. The sphere delimited by radius $r_\theta = r_\mathrm{p} + \theta$ is called the limiting sphere. The surface of the limiting sphere is assumed to be at temperature and species concentration T_θ and C_θ, respectively. Immediately at the particle surface, the temperature and concentration are T_p and C_p, and in the bulk gas, they are T_g and C_g. The gradients between the particle surface and the limiting sphere give rise to heat and mass transport described by free-molecular laws, and the gradients beyond the limiting sphere result in heat and mass transport described by continuum laws. The Knudsen layer is assumed to be in quasi-steady equilibrium, hence energy and mass conservation provide necessary conditions for flux matching at the two interfaces: $\dot{m}_\mathrm{FM} = \dot{m}_\mathrm{C}$ and $\dot{Q}_\mathrm{FM} = \dot{Q}_\mathrm{C}$. Using Equations 3.6, 3.8, 3.9, and 3.10, this resolves to:

$$\alpha_\mathrm{M}\pi r_\mathrm{p}^2(C_\theta\bar{c}_\theta - C_\mathrm{p}\bar{c}_\mathrm{p}) = 4\pi(r_\mathrm{p}+\theta)D(C_\mathrm{g}-C_\theta) \tag{3.11}$$

$$\alpha_\mathrm{T}\pi r_\mathrm{p}^2\frac{p_\theta\bar{c}_\theta}{2}\left(\frac{\gamma+1}{\gamma-1}\right)\left(\frac{T_\mathrm{p}}{T_\theta}-1\right) = 4\pi(r_\mathrm{p}+\theta)k_\mathrm{g}(T_\mathrm{p}-T_\theta) \tag{3.12}$$

where the density ρ in Equation 3.6 was equivalently replaced by the concentration C, and the subscripts g, θ, p respectively denote in the bulk gas, at the limiting sphere surface, and at the particle surface. The boundary sphere method seeks the thickness of the Knudsen layer θ, as well as the temperature and species concentration T_θ and C_θ at the jump distance which allow to satisfy the conservation laws. In the case of combustion of a particle, two additional equations allowing to solve for T_p and C_p are introduced: one for the heat generation rate from the particle, and one for the consumption rate of oxidizer. The flux matching condition of the boundary sphere method

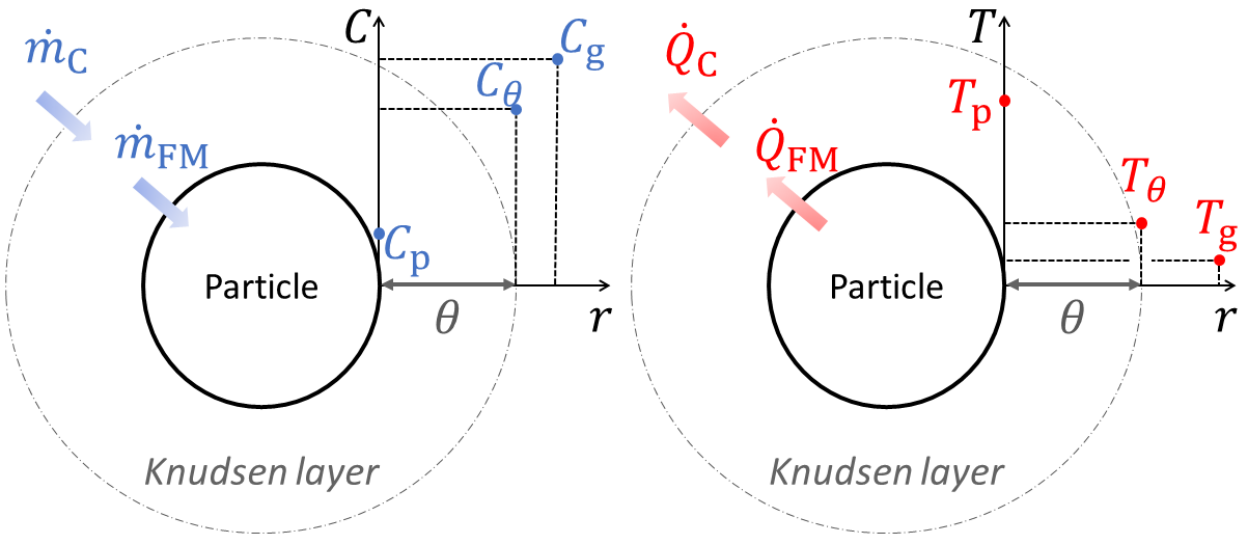

Figure 3.3: Boundary sphere method heat and mass transport. A Knudsen layer of thickness θ proportional to the mean free path is introduced. Subscript θ denotes oxidizer concentration and temperature at the edge of the layer. FM denotes free-molecular, and C denotes continuum.

involves solving a system of coupled nonlinear equations to resolve the properties at the limiting sphere interface and at the particle surface.

The boundary sphere method is most sophisticated in that it imposes no restrictions on the temperature and concentration differences between the particle and the bulk gas, while several other methods for example implicitly assume small temperature difference [15]. This feature allows application of this method to a wide variety of problems such as laser-induced incandescence conduction, particle combustion in the kinetic- of diffusive- limited regime, and droplet evaporation problems. As well, the boundary sphere formulation allows to take into account the variation of thermal and mass transport properties k_g and D through the transport regions. This method also yields the correct solutions in the free-molecular and the continuum limits.

The primary difficulty of the boundary sphere method resides in determining the appropriate Knudsen layer thickness θ for the flux matching conditions. The perhaps most widely applied formulation was provided by Wright [41] in a derivation based on the Knudsen cosine law, which takes into account particle curvature effects to calculate the effective collision-less region governed by free-molecular transport. However, the exact formulation of θ is shown to yield only marginal

variations of the flux rates and final problem solution, provided that it is a factor close to unity of the mean free path [15, 36].

The boundary sphere method is implicit in that it requires solving a coupled system of nonlinear equations to extract the transition effects on the heat and mass fluxes. Under certain assumptions, the heat transport rate can be expressed in an explicit form by applying a transitional correctional factor to the continuum transport rate. Liu et al. [15] derived such a formulation based on the Springer & Tsai [45] model:

$$\frac{\dot{Q}}{\dot{Q}_{\mathrm{C}}} = \left(\frac{1}{1 + \mathrm{Kn}} + \frac{(9\gamma - 5)\mathrm{Kn}}{\alpha_{\mathrm{T}}(\gamma + 1)} \right)^{-1}. \tag{3.13}$$

where $\dot{Q}$ is the actual heat transfer rate and $\dot{Q}_{\mathrm{C}} = 4\pi r_{\mathrm{p}} k_{\mathrm{g}} (T_{\mathrm{p}} - T_{\mathrm{g}})$ is the continuum solution. The Knudsen number is based on the mean free path of the bulk gas. As well, Equation 3.13 assumes small temperature difference $T_{\mathrm{p}} \approx T_{\mathrm{g}}$, and formulates the Knudsen layer thickness as equal to the mean free path of the bulk gas $\theta = \lambda_{\mathrm{MFP,g}}$.

3.3.2 Explicit Solution - Transitional Correction Factors

Multiple authors attempt a solution of the rigorous Boltzmann transport equation to describe the heat and mass transport rates in the transitional regime using transitional corrections factor. These solutions typically imply a linearization of the collision term of the Boltzmann equation proposed by Bhatnagar et al. [46] (BGK model). A solution achieved by Smirnov with a modification proposed by Fuchs is reported by Wagner [38], where the mass and thermal transport transitional correction factors β_{M} and β_{T} are:

$$\beta_{\mathrm{M}} = \frac{\dot{m}}{\dot{m}_{\mathrm{C}}} = \frac{1 + \mathrm{Kn}}{1 + (\frac{4}{3\alpha_{\mathrm{M}}} + 0.377)\mathrm{Kn} + \frac{4}{3\alpha_{\mathrm{M}}}\mathrm{Kn}^2} \tag{3.14}$$

$$\beta_{\mathrm{T}} = \frac{\dot{Q}}{\dot{Q}_{\mathrm{C}}} = \frac{1 + \mathrm{Kn}}{1 + (\frac{4}{3\alpha_{\mathrm{T}}} + 0.377)\mathrm{Kn} + \frac{4}{3\alpha_{\mathrm{T}}}\mathrm{Kn}^2}. \tag{3.15}$$

The actual mass and heat transport rates are $\dot{m}$ and $\dot{Q}$, and the continuum rates $\dot{m}_{\mathrm{C}}$ and $\dot{Q}_{\mathrm{C}}$ are those described by Equations 3.9 and 3.10. The above expressions are valid for arbitrary Knudsen number.

Wagner [38] reports that different Knudsen numbers are used for the thermal and mass transport transitional correction factors in evaporation problems. For the thermal transport, the Knudsen number is based on the mean free path of the bulk gas, and for the mass transport, it is based on the mean free path of the droplet vapor. In the intended combustion problem of the current work, thermal and mass transport occur from the bulk gas towards the particle surface. As such, the mean free path of the bulk gas is used in both cases.

Chapter 4

Model Formulation - Isolated Iron Particle

Given tools to describe the kinetics of iron oxidation and transport processes across the entire range of Knudsen number, a model which implements the effect of the Knudsen layer on the transport rates is formulated to evaluate the ignition behavior of fine iron particles across the Knudsen transition regime. The current analysis implements a thermophysical model for single iron particle ignition based on: the mass and energy balance equations; the empirically calibrated parabolic kinetic model of iron oxidation [3]; a switch-type transition model between the kinetic- and diffusive-limited combustion regimes; and a two-layer boundary sphere approach to account for transition transport effects on heat and mass transfer. The current chapter details the model formulation and lists the major assumptions used in the analysis.

4.1 Model Description

The model considers a spherical particle consisting of an iron core of radius r_{Fe}, an inner FeO layer of thickness X_{FeO}, an outer Fe_3O_4 layer of thickness $X_{\mathrm{Fe_3O_4}}$, and a Knudsen layer of thickness θ, as illustrated in Figure 4.1. The particle is placed in a binary gas mixture consisting of oxygen and an inert gas. The particle exchanges heat and mass to the surrounding Knudsen layer through free-molecular transport, and continuum transport describes heat and mass transport beyond the

Knudsen layer surface. Heat transfer is considered to occur only through conduction - radiative heat transfer is neglected, as it is shown to have a negligible impact on particle ignition temperature [3]. Other major assumptions used in this formulation include:

1. The thermal expansion of Fe, FeO, and Fe_3O_4 is neglected, and the solids maintain a constant density throughout the burn ρ_{Fe}, ρ_{FeO}, and $\rho_{\text{Fe}_3\text{O}_4}$, respectively.
2. The particle is assumed to be at a uniform temperature T_{p}.
3. The bulk gas is in sufficient quantity such that its properties, including temperature and oxidizer concentration, are not affected by the burning particle.
4. The flow velocity of the ambient gas is negligible.
5. The Stefan flow induced by the consumption of oxidizer at the particle surface is neglected.
6. The second-order heat and mass transport mechanisms, the Dufour effect and the Soret effect, are neglected.
7. The Knudsen layer is quasi-steady.

The state vector $\mathbf{x} = \begin{bmatrix} M_{\text{Fe}} & M_{\text{FeO}} & M_{\text{Fe}_3\text{O}_4} & H_{\text{p}} \end{bmatrix}^{\mathbf{T}}$ tracks the particle mass content in Fe, mass content in FeO, mass content in Fe_3O_4, and the total particle internal energy (or enthalpy), respectively. The internal energy of the particle is:

$$H_{\text{p}} = \sum_{i}^{N_{\text{s}}} M_i h_i(T_{\text{p}}) \tag{4.1}$$

where i is the index of the solid-phase species, N_{s} is the number of solid-phase species, and h_i is the particle gravimetric enthalpy. The latter is computed as a function of particle temperature T_{p} and molar weight of the species W_i, using the Shomate equation based on the NIST Standard Reference Database [47]. The formulations of the Shomate polynomials are provided in Appendix A. While tracking the particle enthalpy, an iterative root-finding procedure can be used to determine the

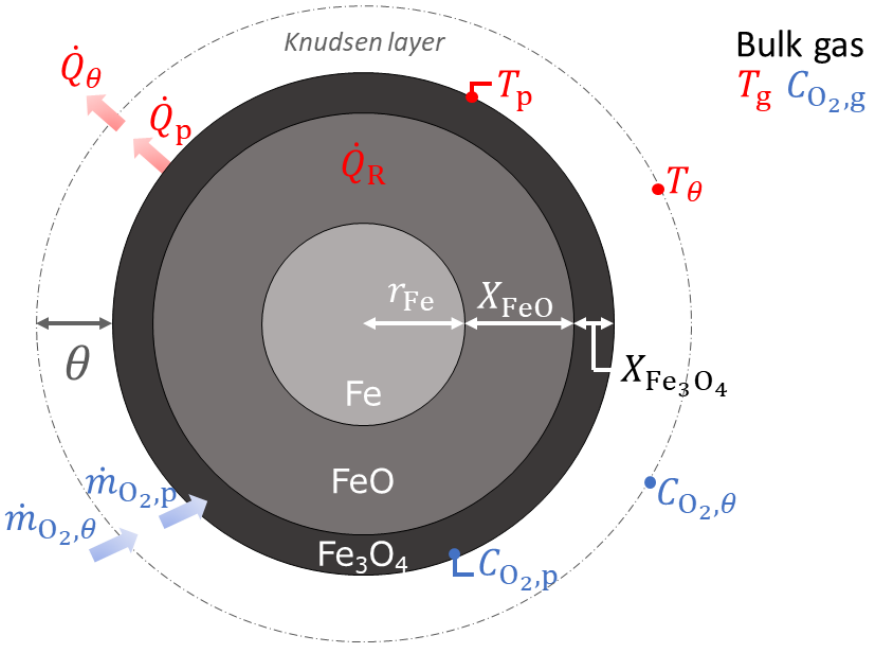

Figure 4.1: Particle reaction model. Symbols T and C_{O_2} denote temperature and oxidizer concentration. Subscripts p, θ, and g denote particle surface, limiting sphere surface, and bulk gas. Heat and mass transport $\dot{Q}$, $\dot{m}_{O_2}$ are respectively governed by free-molecular and continuum laws inside and beyond the Knudsen layer of thickness θ.

particle temperature T_p. The formation of the oxides are described by the stoichiometric reactions:

$$1\ \text{Fe} + 1/2\ \text{O}_2 \rightarrow 1\ \text{FeO}$$

$$3\ \text{Fe} + 2\ \text{O}_2 \rightarrow 1\ \text{Fe}_3\text{O}_4$$

4.2 Conservation Laws in the Quasi-Steady Knudsen Layer

4.2.1 Heat Balance

The heat balance in the quasi-steady Knudsen layer is described by $\dot{Q}_p = \dot{Q}_\theta$, where $\dot{Q}_p$ represents the free-molecular conductive heat loss rate from the particle to the Knudsen layer, and $\dot{Q}_\theta$ represents the continuum conductive heat loss rate from the Knudsen layer to the bulk gas. In the

free-molecular regime, the heat loss rate is described by [15]:

$$\dot{Q}_{\mathrm{p}} = \alpha_{\mathrm{T}} \pi r_{\mathrm{p}}^2 \frac{p\bar{c}_\theta}{2} \left(\frac{\gamma+1}{\gamma-1}\right)^* \left(\frac{T_{\mathrm{p}}}{T_\theta} - 1\right) \tag{4.2}$$

where α_{T} is the thermal accommodation coefficient; r_{p} is particle radius; p, $\bar{c}_\theta$, and T_θ are respectively pressure, mean molecular speed, and gas temperature at the Knudsen layer surface; and γ is the gas specific heat ratio. As the particle reacts in an open stream, the pressure p is spatially and temporally uniform.

The thermal accommodation coefficient is a function of multiple surface parameters, such as adsorbed gas layers on the particle and surface roughness [25, 32–35]. In the current analysis, the surface is assumed to be smooth, and the Song & Yovanovich [33] semi-empirical correlation is used to calculate α_{T}:

$$\alpha_{\mathrm{T}} = A\left(\frac{W_{\mathrm{g}}^*}{6.80 + W_{\mathrm{g}}^*}\right) + (1-A)\left(\frac{2.40B}{(1+B)^2}\right) \tag{4.3}$$

$$W_{\mathrm{g}}^* = 1.40 N_{\mathrm{A}} m_\theta \tag{4.4}$$

$$A = \exp\left[-0.57\left(\frac{T_{\mathrm{p}} - 273}{273}\right)\right] \tag{4.5}$$

$$B = \frac{N_{\mathrm{A}} m_\theta}{W_{\mathrm{Fe_2O_3}}} \tag{4.6}$$

where $m_\theta = (\sum_i^{N_{\mathrm{g}}} C_{i,\theta} m_i)/(\sum_i^{N_{\mathrm{g}}} C_{i,\theta})$ is the average individual molecular mass at the Knudsen layer surface, with $C_{i,\theta}$ the concentration of the ith species at the Knudsen layer surface, m_i its individual molecular mass, and N_{g} the total number of gaseous species; $W_{\mathrm{Fe_2O_3}}$ is the molar weight of Fe_2O_3; and N_{A} is Avogadro's number. Although Fe_2O_3 is not considered in the thermophysical analysis, it is used to compute α_{T}, which is a surface property. The thermal accommodation coefficient semi-empirical correlation is compared to experimental data for different Fe-gas systems in Appendix B. There is high scatter in the literature-reported values of α_{T}. However as demonstrated in Appendix B, although the exact quantitative values of the ignition temperatures are affected by α_{T}, the overall conclusions attained in the current work remain unchanged for values within the confidence interval 0.08-0.90 of the literature data.

The pressure at the Knudsen layer surface p is the sum of the partial pressures of the gas species:

$$p = k_{\mathrm{B}} T_\theta \sum_i^{N_{\mathrm{g}}} \frac{C_{i,\theta}}{m_i} \tag{4.7}$$

where k_{B} is the Boltzmann constant. As the pressure is spatially and temporally constant, the inert gas concentration at the Knudsen layer surface can be computed from Equation 4.7, given $C_{\mathrm{O}_2,\theta}$ and T_θ. The average molecular speed $\bar{c}_\theta$ arises from Boltzmann gas kinetics theory [25]:

$$\bar{c}_\theta = \sqrt{\frac{8 k_{\mathrm{B}} T_\theta}{\pi m_\theta}}. \tag{4.8}$$

The exact formulation for $\left(\frac{\gamma+1}{\gamma-1}\right)^*$ considers the varying thermophysical properties of the gas arising from the concentration and temperature gradients in the Knudsen layer:

$$\left(\frac{\gamma+1}{\gamma-1}\right)^* = \left(\frac{1}{T_{\mathrm{p}} - T_\theta}\right)\left(\frac{1}{C_{\mathrm{O}_2,\mathrm{p}} - C_{\mathrm{O}_2,\theta}}\right) \int_{T_\theta}^{T_{\mathrm{p}}} \int_{C_{\mathrm{O}_2,\theta}}^{C_{\mathrm{O}_2,\mathrm{p}}} \left(\frac{\gamma(C_{\mathrm{O}_2}, T)+1}{\gamma(C_{\mathrm{O}_2}, T)-1}\right) \mathrm{d}C_{\mathrm{O}_2}\, \mathrm{d}T. \tag{4.9}$$

In the current analysis, the specific heat ratio $\gamma_{\mathrm{p}}^*(C_{\mathrm{O}_2,\mathrm{p}}^*, T_{\mathrm{p}}^*)$ is instead computed using a two-thirds law: the oxidizer concentration and the gas temperature are taken to be a weighted average of two thirds the values at the particle surface, and one third the values at the Knudsen layer surface. These are denoted by the notation $C_{\mathrm{O}_2,\mathrm{p}}^*$ and T_{p}^*. The specific heat ratio γ_{p}^* is then calculated at these two-thirds weighted values for the gas mixture, and Equation 4.9 reduces to:

$$\left(\frac{\gamma+1}{\gamma-1}\right)^* = \frac{\gamma_{\mathrm{p}}^*+1}{\gamma_{\mathrm{p}}^*-1}. \tag{4.10}$$

The two-thirds law approach significantly reduces numerical implementation complexity, while maintaining a high accuracy of the results for heterogeneous reaction mechanisms [48]. As discussed in Section 3.2.3, the gradients of T and C change rapidly while approaching the wall due to the jump conditions induced by the Knudsen layer, hence the thermal properties should be taken closer to the wall temperature and oxidizer concentration, justifying the two-thirds law. In Equation

4.10, the heat capacity ratio is approximated as:

$$\gamma_{\mathrm{p}}^{*} = \frac{c_{p,\mathrm{p}}^{*}}{c_{p,\mathrm{p}}^{*} - \frac{R_{\mathrm{u}}}{N_{\mathrm{A}} m_{\mathrm{p}}^{*}}} \tag{4.11}$$

where $c_{p,\mathrm{p}}^{*}$ is the gravimetric specific heat capacity of the gas mixture computed at $C_{\mathrm{O_2,p}}^{*}$ and T_{p}^{*}; R_{u} is the universal gas constant; and m_{p}^{*} is the average gas individual molecular mass computed at $C_{\mathrm{O_2,p}}^{*}$. The specific heat capacity of a gas mixture is the weighted average of the specific heat capacity of each species, $c_{p,\mathrm{p}}^{*} = \left[\sum_i^{N_{\mathrm{g}}} C_{i,\mathrm{p}}^{*} c_{p,i}(T_{\mathrm{p}}^{*})\right] / \left[\sum_i^{N_{\mathrm{g}}} C_{\mathrm{i},p}^{*}\right]$. The species' specific heat capacities are obtained using the 7-coefficient NASA-polynomials [40], evaluated at temperature T_{p}^{*}. Coefficients and formulations are provided in Appendix A.

In the continuum regime, the heat transfer rate from the Knudsen layer to the bulk gas is described by [15]:

$$\dot{Q}_{\theta} = 4\pi(r_{\mathrm{p}} + \theta) k_{\mathrm{g},\theta}^{*} (T_{\theta} - T_{\mathrm{g}}) \tag{4.12}$$

where $k_{\mathrm{g},\theta}^{*}$ is the thermal conductivity averaged between the bulk gas and the Knudsen layer surface. The exact formulation of the Knudsen layer thickness derived by Wright [41] is:

$$\theta = \frac{r_{\mathrm{p}}^{3}}{\lambda_{\mathrm{MFP},\theta}^{2}} \left(\frac{1}{5}\Lambda_1^5 - \frac{1}{3}\Lambda_1^3 \Lambda_2 + \frac{2}{15}\Lambda_2^{5/2} \right) - r_{\mathrm{p}} \tag{4.13}$$

$$\Lambda_1 = 1 + \frac{\lambda_{\mathrm{MFP},\theta}}{r_{\mathrm{p}}} \tag{4.14}$$

$$\Lambda_2 = 1 + \left(\frac{\lambda_{\mathrm{MFP},\theta}}{r_{\mathrm{p}}} \right)^{2} \tag{4.15}$$

where $\lambda_{\mathrm{MFP},\theta}$ is the mean free path at the Knudsen layer surface. However, as mentioned in Section 3.3.1, the exact formulation of θ only mildly affects the transport rates. The current analysis therefore employs $\theta = \lambda_{\mathrm{MFP,g}}$ as an approximation, taking advantage of the constant properties of the bulk gas throughout the burn. The molecular mean free path is formulated as [15]:

$$\lambda_{\mathrm{MFP,g}} = \frac{k_{\mathrm{g,g}}}{f_{\mathrm{g}}\, p} (\gamma_{\mathrm{g}} - 1) \sqrt{\frac{\pi m_{\mathrm{g}} T_{\theta}}{2 k_{\mathrm{B}}}} \tag{4.16}$$

where $k_{\mathrm{g,g}}$ is the mixture-averaged thermal conductivity in the bulk gas, and $f_{\mathrm{g}} = \frac{(9\gamma_{\mathrm{g}}-5)}{4}$ is the Eucken factor. The following approximation is used to compute the mixture-averaged thermal conductivity, based on the species thermal conductivity k_i and their mole fractions μ_i:

$$k_{\mathrm{g}} = \frac{1}{2}\left(\sum_{i}^{N_{\mathrm{g}}} \mu_i k_i + \frac{1}{\sum_{i}^{N_{\mathrm{g}}} \mu_i / k_i} \right). \tag{4.17}$$

The species' thermal conductivity are evaluated using the NASA 5-coefficients polynomials as a function of temperature [40], as detailed in Appendix A. In Equation 4.12, the exact formulation for the averaged thermal conductivity between the bulk gas and the Knudsen layer surface is:

$$k^*_{\mathrm{g},\theta} = \left(\frac{1}{T_\theta - T_{\mathrm{g}}}\right)\left(\frac{1}{C_{\mathrm{O_2},\theta} - C_{\mathrm{O_2,g}}}\right) \int_{T_{\mathrm{g}}}^{T_\theta} \int_{C_{\mathrm{O_2,g}}}^{C_{\mathrm{O_2},\theta}} k_{\mathrm{g}}(C_{\mathrm{O_2}}, T) \mathrm{d}C_{\mathrm{O_2}}\, \mathrm{d}T. \tag{4.18}$$

To simplify numerical implementation, a two-thirds law is instead used to compute $k^*_{\mathrm{g},\theta}$: the temperature and oxidizer concentration are taken as two thirds the values at the Knudsen layer surface and one third the values in the bulk gas, denoted T^*_θ and $C^*_{\mathrm{O_2},\theta}$. The species' thermal conductivity is then computed with the NASA polynomials, and Equation 4.17 is used to obtain the mixture-averaged thermal conductivity.

4.2.2 Mass Balance

The mass balance in the quasi-steady Knudsen layer is $\dot{m}_{\mathrm{O_2,p}} = \dot{m}_{\mathrm{O_2},\theta}$ The mass consumption of oxidizer at the particle surface in the free-molecular regime is described by (Section 3.2.1):

$$\dot{m}_{\mathrm{O_2,p}} = \alpha_{\mathrm{M}} \pi r_{\mathrm{p}}^2 (C_{\mathrm{O_2},\theta}\, \bar{c}_\theta - C_{\mathrm{O_2,p}}\, \bar{c}_{\mathrm{p}}) \tag{4.19}$$

where α_{M} is the mass accommodation coefficient, which is in practice a transient function of temperature and oxidizer coverage at the particle surface [14,27–31]. In the current analysis, α_{M} is set constant at a value of 0.10, which is in the correct order of magnitude for iron-oxygen systems reported in the above-mentioned sources. In Appendix B, a parametric study of the impact of α_{M}

on the ignition temperature is performed. Reasonable values of α_{M} are found to yield no impact on the ignition temperature.

At the limiting sphere surface, diffusion in the continuum regime is described by Fick's law:

$$\dot{m}_{\mathrm{O_2},\theta} = 4\pi(r_{\mathrm{p}} + \theta) D^*_\theta (C_{\mathrm{O_2,g}} - C_{\mathrm{O_2},\theta}). \tag{4.20}$$

The mass diffusion coefficient D^*_θ is computed as the average binary diffusivity of oxidizer in the inert gas across the limiting sphere. The Fuller-Schettler-Giddins semi-empirical correlation is used to approximate the binary diffusion coefficient [49]:

$$D = \frac{10^{-7} T^{1.75} \left[\frac{W_{\mathrm{inert}} + W_{\mathrm{O_2}}}{W_{\mathrm{inert}} W_{\mathrm{O_2}}}\right]^{1/2}}{\frac{p}{101325}\left[\left(\sum v\right)_{\mathrm{O_2}}^{1/3} + \left(\sum v\right)_{\mathrm{inert}}^{1/3}\right]^2}. \tag{4.21}$$

The terms $\left(\sum v\right)_i$ are semi-empirical parameters used for the correlation and are provided in Appendix A. Equation 4.21 was modified from [49] for the result to be obtained in $\mathrm{m^2 s^{-1}}$, and assuming the units of p are Pa instead of atm. To take into account the temperature gradient from the bulk gas to the Knudsen layer, the exact formulation for D^*_θ would require averaging by integration Equation 4.21 across temperature. Instead T is replaced by T^*_θ, implementing the two-thirds law.

4.3 Oxidizer Consumption Rate

The interplay between kinetic- and diffusion- limited combustion of the iron particle is implemented by comparing the instantaneous maximum possible oxygen diffusion rate (assuming $C_{\mathrm{O_2,p}} = 0$), to the maximum instantaneous kinetic consumption rate of oxidizer (from parabolic kinetic laws). The lowest of these two values is assumed to be the instantaneous oxidizer consumption rate, and resulting reaction rates for Fe, FeO, and Fe_3O_4 are computed.

4.3.1 Kinetic-Limited Regime

In the kinetic-limited regime, the parabolic kinetic model [3] governs the rate of production of FeO ($\dot{m}_{\text{FeO,kin}}$) and Fe_3O_4 ($\dot{m}_{\text{Fe}_3\text{O}_4\text{,kin}}$), and the rate of consumption of Fe ($\dot{m}_{\text{Fe,kin}}$):

$$\dot{m}_{\text{Fe,kin}} = -\nu_{\text{Fe/FeO}}\dot{m}_{\text{FeO,kin}} - \nu_{\text{Fe/Fe}_3\text{O}_4}\dot{m}_{\text{Fe}_3\text{O}_4\text{,kin}} \tag{4.22}$$

$$\dot{m}_{\text{FeO,kin}} = \rho_{\text{FeO}} A_{\text{FeO}} \frac{\mathrm{d}X_{\text{FeO}}}{\mathrm{d}t} \tag{4.23}$$

$$\dot{m}_{\text{Fe}_3\text{O}_4\text{,kin}} = \rho_{\text{Fe}_3\text{O}_4} A_{\text{Fe}_3\text{O}_4} \frac{\mathrm{d}X_{\text{Fe}_3\text{O}_4}}{\mathrm{d}t} \tag{4.24}$$

where $\nu_{\text{Fe/FeO}}$ and $\nu_{\text{Fe/Fe}_3\text{O}_4}$ are stoichiometric mass ratios; $A_{\text{FeO}} = 4\pi(r_{\text{Fe}} + X_{\text{FeO}})^2$ is the area of formation of FeO; and $A_{\text{Fe}_3\text{O}_4} \equiv A_{\text{p}} = 4\pi r_{\text{p}}^2$ is the area of formation of Fe_3O_4. The kinetic growth rates of the iron oxide layers thicknesses are:

$$\frac{\mathrm{d}X_i}{\mathrm{d}t} = \frac{k_{0,i}}{X_i} \exp\left(\frac{-T_{\text{a},i}}{T_{\text{p}}}\right). \tag{4.25}$$

Kinetic parameters $k_{0,i}$ and $T_{\text{a},i}$ are provided in Section 4.5. The resulting kinetic consumption rate of oxidizer by the particle is computed from the stoichiometric mass ratios:

$$\dot{m}_{\text{O}_2\text{,kin}} = \nu_{\text{O}_2\text{/FeO}}\dot{m}_{\text{FeO,kin}} + \nu_{\text{O}_2\text{/Fe}_3\text{O}_4}\dot{m}_{\text{Fe}_3\text{O}_4\text{,kin}}. \tag{4.26}$$

4.3.2 Diffusive-Limited Regime

In the diffusive-limited regime, the consumption rate of oxidizer is equal to its maximum possible transport rate through the Knudsen layer:

$$\dot{m}_{\text{O}_2\text{,diff}} = \alpha_{\text{M}}\pi r_{\text{p}}^2 (C_{\text{O}_2,\theta}\bar{c}_\theta). \tag{4.27}$$

The O_2 is partitioned in FeO and Fe_3O_4 based on the instantaneous kinetic rates from Equations 4.23, 4.24, and 4.26:

$$R_{\text{FeO}} = \nu_{\text{O}_2/\text{FeO}} \frac{\dot{m}_{\text{FeO,kin}}}{\dot{m}_{\text{O}_2,\text{kin}}} \tag{4.28}$$

$$R_{\text{Fe}_3\text{O}_4} = 1 - R_{\text{FeO}} \tag{4.29}$$

where R_{FeO} is the fraction of O_2 consumed to produce FeO, and $R_{\text{Fe}_3\text{O}_4}$ is the fraction consumed to produce Fe_3O_4. The rates in the diffusive-limited regime are then:

$$\dot{m}_{\text{FeO,diff}} = R_{\text{FeO}} \dot{m}_{\text{O}_2,\text{diff}} \left(\frac{1}{\nu_{\text{O}_2/\text{FeO}}} \right) \tag{4.30}$$

$$\dot{m}_{\text{Fe}_3\text{O}_4,\text{diff}} = R_{\text{Fe}_3\text{O}_4} \dot{m}_{\text{O}_2,\text{diff}} \left(\frac{1}{\nu_{\text{O}_2/\text{Fe}_3\text{O}_4}} \right) \tag{4.31}$$

$$\dot{m}_{\text{Fe,diff}} = -\nu_{\text{Fe}/\text{FeO}} \dot{m}_{\text{FeO,diff}} - \nu_{\text{Fe}/\text{Fe}_3\text{O}_4} \dot{m}_{\text{Fe}_3\text{O}_4,\text{diff}}. \tag{4.32}$$

4.4 Governing Equations

The governing equations for the rate of change of the state variables are:

$$\frac{\mathrm{d}M_{\text{Fe}}}{\mathrm{d}t} = \dot{m}_{\text{Fe}} \tag{4.33}$$

$$\frac{\mathrm{d}M_{\text{FeO}}}{\mathrm{d}t} = \dot{m}_{\text{FeO}} \tag{4.34}$$

$$\frac{\mathrm{d}M_{\text{Fe}_3\text{O}_4}}{\mathrm{d}t} = \dot{m}_{\text{Fe}_3\text{O}_4} \tag{4.35}$$

$$\frac{\mathrm{d}H_{\text{p}}}{\mathrm{d}t} = q_{\text{FeO}} \frac{\mathrm{d}M_{\text{FeO}}}{\mathrm{d}t} + q_{\text{Fe}_3\text{O}_4} \frac{\mathrm{d}M_{\text{Fe}_3\text{O}_4}}{\mathrm{d}t} + h_{\text{O}_2,\theta} \dot{m}_{\text{O}_2} - \dot{Q}_{\text{p}}. \tag{4.36}$$

Equations 4.33 to 4.35, as well as $\dot{m}_{\text{O}_2}$ in Equation 4.36 are computed either in the kinetic- or diffusive- limited regime, depending on which mechanism instantaneously limits the reaction rates. In Equation 4.36, the first two terms on the right-hand side are the energy release rates due to the formation of FeO and Fe_3O_4 respectively, where q_{FeO} and $q_{\text{Fe}_3\text{O}_4}$ are the specific heating values of the oxides. The third term relates to the enthalpy increase of the particle due to the incorporation

of O_2, where $h_{O_2,\theta}$ is the gravimetric enthalpy of oxygen evaluated at T_θ. The last term is the heat loss rate from the particle to the Knudsen layer, as described by Equation 4.2.

4.5 Numerical Implementation

The single particle model is numerically implemented in MATLAB. The problem is initialized by providing the following parameters:

- T_{g}, bulk gas temperature;
- p, bulk gas pressure (1 atm);
- $r_{\mathrm{p},0}$, initial particle radius;
- δ_0, initial oxide layer thickness ratio.

To represent air, the bulk gas mixture is set to be 21% O_2 and 79% N_2 on a molar basis. The initial particle temperature $T_{\mathrm{p},0}$ is initialized to be equal to the gas temperature: $T_{\mathrm{p},0} = T_{\mathrm{g}}$. The initial oxide layer thickness ratio δ_0, and the ratio between the Fe_3O_4 layer thickness to the total oxide layer thickness $\delta_{0,\mathrm{Fe_3O_4}}$ are defined as:

$$\delta_0 = \frac{X_0}{r_{\mathrm{p},0}} \equiv \frac{X_{\mathrm{FeO},0} + X_{\mathrm{Fe_3O_4},0}}{r_{\mathrm{p},0}} \tag{4.37}$$

$$\delta_{0,\mathrm{Fe_3O_4}} = \frac{X_{\mathrm{Fe_3O_4},0}}{X_0} \tag{4.38}$$

The variable δ_0 can be related to $m_{\mathrm{oxides}}/m_{\mathrm{total}}$, the ratio of the mass of iron oxides to the total mass of solid species, which are experimentally measurable quantities. In the current analysis, a constant value of $\delta_{0,\mathrm{Fe_3O_4}} = 0.05$ is used, as inferred from experimental measurements [22]. From the initial particle dimensions and temperature, the initial state vector $\mathbf{x_0}$ can be computed.

From the detailed description of the heat and mass balance in the quasi-steady Knudsen layer provided in Section 4.2, the following system of three equations, three unknowns can be written:

$$\alpha_{\mathrm{T}}\pi r_{\mathrm{p}}^2\frac{p\bar{c}_\theta}{2}\left(\frac{\gamma_{\mathrm{p}}^*+1}{\gamma_{\mathrm{p}}^*-1}\right)\left(\frac{T_{\mathrm{p}}}{T_\theta}-1\right) = 4\pi(r_{\mathrm{p}}+\theta)k_{\mathrm{g},\theta}^*(T_\theta-T_{\mathrm{g}}) \tag{4.39}$$

$$\dot{m}_{\mathrm{O_2}} = \alpha_{\mathrm{M}}\pi r_{\mathrm{p}}^2(C_{\mathrm{O_2},\theta}\,\bar{c}_\theta - C_{\mathrm{O_2,p}}\,\bar{c}_{\mathrm{p}}) \tag{4.40}$$

$$\dot{m}_{\mathrm{O_2}} = 4\pi(r_{\mathrm{p}}+\theta)D_\theta^*(C_{\mathrm{O_2,g}}-C_{\mathrm{O_2},\theta}). \tag{4.41}$$

The three unknowns of the system depend on whether the particle burns in the kinetic- or the diffusive- limited regime. In the kinetic-limited regime, the consumption rate of oxygen $\dot{m}_{\mathrm{O_2}} = \dot{m}_{\mathrm{O_2,kin}}$ is known from Equation 4.26 and associated relations, which only require knowledge of the instantaneous state vector $\mathbf{x}$. In this case, the unknowns are $\{T_\theta, C_{\mathrm{O_2},\theta}, C_{\mathrm{O_2,p}}\}$. In the case of diffusive-limited combustion, the oxidizer concentration at the particle surface $C_{\mathrm{O_2,p}} = 0$ is known, and the three unknowns are $\{T_\theta, C_{\mathrm{O_2},\theta}, \dot{m}_{\mathrm{O_2}}\}$. The reader can refer to Appendix C for the detailed derivation of the numerical solution to the system.

The state vector is advanced in time using the governing equations described by Equations 4.33 to 4.35. At each time step, the consumption and production rates are determined by comparing $\dot{m}_{\mathrm{O_2,kin}}$ to $\dot{m}_{\mathrm{O_2,diff}}$. The actual consumption rate of oxygen $\dot{m}_{\mathrm{O_2}}$ is chosen to be the lowest of the two. Then, $\dot{m}_{\mathrm{Fe}}$, $\dot{m}_{\mathrm{FeO}}$, and $\dot{m}_{\mathrm{Fe_3O_4}}$ are computed either in the kinetic- or diffusive- limited regime with appropriate relations. Once the system described by Equations 4.39 to 4.41 is solved, instantaneous parameters T_θ and $C_{\mathrm{O_2},\theta}$ are known, allowing to obtain $\dot{Q}_{\mathrm{p}}$ from either side of Equation 4.39. This allows to compute the result of Equation 4.36 and advance $\mathbf{x}$ in time. The governing equations are solved for a determined duration of time, until $M_{\mathrm{Fe}}/M_{\mathrm{Fe,0}} \leq 1/100$, or until the melting point of FeO is reached (1650 K), in which case the particle undergoes thermal runaway. The MATLAB solver *ode15s* is used to solve the system of first-order ordinary differential equations. Table 4.1 provides properties and parameters used in the current analysis.

Table 4.1: Properties and kinetic parameters of Fe, FeO, and Fe_3O_4.

Description	Symbol	Value	Units
Density	ρ_{Fe}	7874	kg/m^3
	ρ_{FeO}	5745	
	$\rho_{Fe_3O_4}$	5170	
Specific heating value	q_{FeO}	3.787	MJ/kg
	$q_{Fe_3O_4}$	4.841	
Kinetic rate constant	$k_{0,FeO}$	2.670 x 10^{-4}	m^2/s
	k_{0,Fe_3O_4}	1.027 x 10^{-6}	
Activation temperature	$T_{a,FeO}$	20319	K
	T_{a,Fe_3O_4}	21310	

4.6 Alternative Solution Methods

The numerical implementation of the fully implicit, complete formulation of the boundary sphere method requires solving a nonlinear system of three equations, three unknowns. This comes with a computational cost, as well as possible errors in the mathematical derivation of the solution. To verify the robustness of the numerical implementation, alternative solution methods are proposed. These methods are compared to the implicit boundary sphere approach in Section 5.1.2.

4.6.1 Transitional Correction Factors

Smirnov's solution to the transport rates in the transition regime is [38]:

$$\beta_{\mathrm{M}} = \frac{\dot{m}}{\dot{m}_{\mathrm{C}}} = \frac{1+\mathrm{Kn}}{1+(\frac{4}{3\alpha_{\mathrm{M}}}+0.377)\mathrm{Kn}+\frac{4}{3\alpha_{\mathrm{M}}}\mathrm{Kn}^2} \tag{4.42}$$

$$\beta_{\mathrm{T}} = \frac{\dot{Q}}{\dot{Q}_{\mathrm{C}}} = \frac{1+\mathrm{Kn}}{1+(\frac{4}{3\alpha_{\mathrm{T}}}+0.377)\mathrm{Kn}+\frac{4}{3\alpha_{\mathrm{T}}}\mathrm{Kn}^2}. \tag{4.43}$$

where $\text{Kn} = \lambda_{\text{MFP,g}}/r_{\text{p}}$ is the instantaneous Knudsen number based on the bulk gas mean free path (see Section 3.3.2). The continuum transport rates are computed as:

$$\dot{Q}_{\text{C}} = 4\pi r_{\text{p}} k_{\text{g}}^{*}(T_{\text{p}} - T_{\text{g}}) \tag{4.44}$$

$$\dot{m}_{\text{C}} = 4\pi r_{\text{p}} D^{*}(C_{\text{O}_2,\text{g}} - C_{\text{O}_2,\text{p}}) \tag{4.45}$$

where k_{g}^{*} and D^{*} are computed using the two-thirds law between the particle and the bulk gas temperatures and oxidizer concentrations. The thermal accommodation coefficient is computed using Equations 4.3 to 4.6, with m_{θ} replaced by the average molecular mass of the bulk gas m_{g}. In the diffusive-limited regime, $C_{\text{O}_2,\text{p}} = 0$ is known, while in the kinetic-limited regime, $\dot{m}_{\text{C}}$ is known. In both cases, the system is fully explicit.

4.6.2 Explicit Boundary Sphere Method

Under the assumption of small temperature difference and using $\theta = \lambda_{\text{MFP,g}}$, Liu et al. [15] formulate an explicit solution to the heat transfer rate in the boundary sphere method:

$$\beta_{\text{T}} = \frac{\dot{Q}}{\dot{Q}_{\text{C}}} = \left(\frac{1}{1 + \text{Kn}} + \frac{(9\gamma - 5)\text{Kn}}{\alpha_{\text{T}}(\gamma + 1)} \right)^{-1}. \tag{4.46}$$

where Kn is based on the mean free path of the bulk gas. The transitional correction factor for the mass transport is taken from Smirnov's formulation (Equation 4.42) in this alternative approach.

Chapter 5

Results and Discussion

The boundary sphere solid-phase transient iron oxidation model with oxide layer growth is solved to quantitatively predict the ignition temperature of fine iron particles while accounting for transition transport effects. The impact of initial particle size $d_{\mathrm{p},0}$ on the ignition temperature is assessed. As well, the impact of the initial oxide layer thickness X_0 and oxide layer thickness ratio δ_0 is investigated. The results are compared to the results predicted by the continuum transport rates approach, as formulated by Mi et al. [3], and an accuracy threshold for the continuum modeling approach is established. The results are also compared to an existing model formulated by Senyurt & Dreizin [18] which implements a steady-state formulation of the boundary sphere method for aluminum, boron, and magnesium particles ignition.

5.1 Sample Results

5.1.1 Transient Behavior and Particle Ignition

Figure 5.1 shows the temperature and oxidizer concentration at the particle surface for a burning particle at different bulk gas temperatures. As the bulk gas temperature is increased, the particle's peak burning temperature increasingly separates from the bulk gas. As the particle heats above the gas temperature, the increasing temperature has en effect of accelerating the particle kinetics.

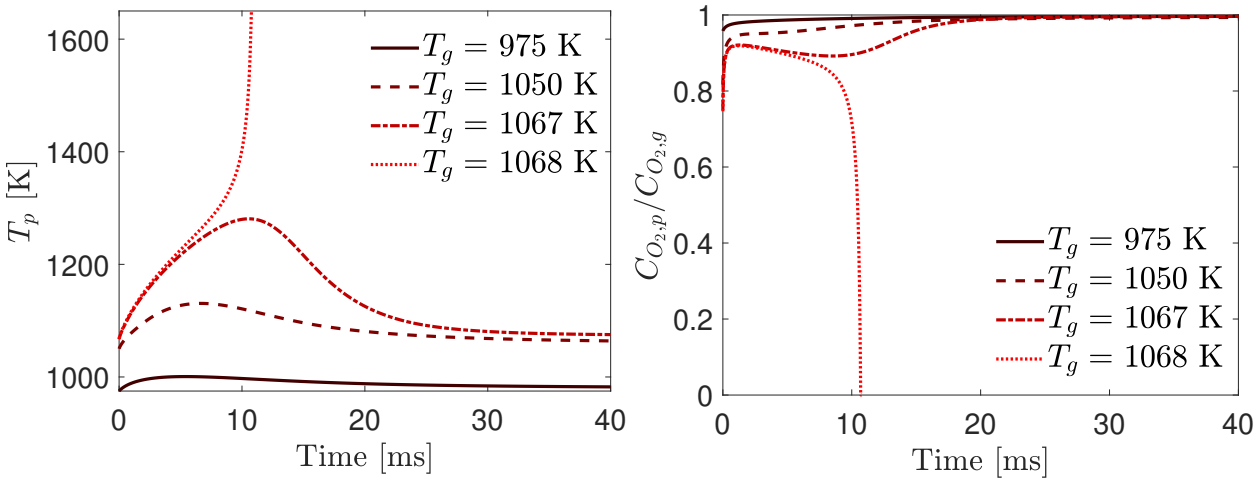

(a) Particle temperature.

(b) Normalized oxidizer concentration.

Figure 5.1: Transient behavior of particle for an initial diameter of 20 μm and an initial oxide layer of 10 nm at different gas temperatures. The particle ignites at $T_{\mathrm{g}} = 1064$ K.

However, the increasing oxide layer thickness on the particle surface has the opposite effect, while also leading to additional thermal mass to be heated by the energy release of the particle. As well, the conductive heat loss rate from the particle increases with the temperature separation. For temperatures below the ignition point, the net result is that the particle's temperature returns close to the bulk gas temperature after reaching a peak and burns in the kinetic-limited regime. This is further confirmed by observing the oxidizer concentration at the particle surface, which stagnates near the bulk gas concentration. At the critical gas temperature for ignition (1069 K), the exponential dependence of the kinetics on temperature exceeds the adverse effect of the oxide layer growth and heat loss rate. The particle transitions to the diffusive-limited regime and ignites, as shown by the oxidizer concentration at the particle surface which reaches 0. The slopes of T_{p} and $C_{\mathrm{O_2,p}}$ at the ignition point are extremely abrupt, demonstrating the near-instantaneous character of the ignition phenomenon.

5.1.2 Comparison of Solution Methods

Figure 5.2 shows the ignition temperature as a function of particle size for a constant oxide layer thickness as resolved by the three different solutions methods outlined in Sections 4.5 and 4.6. The

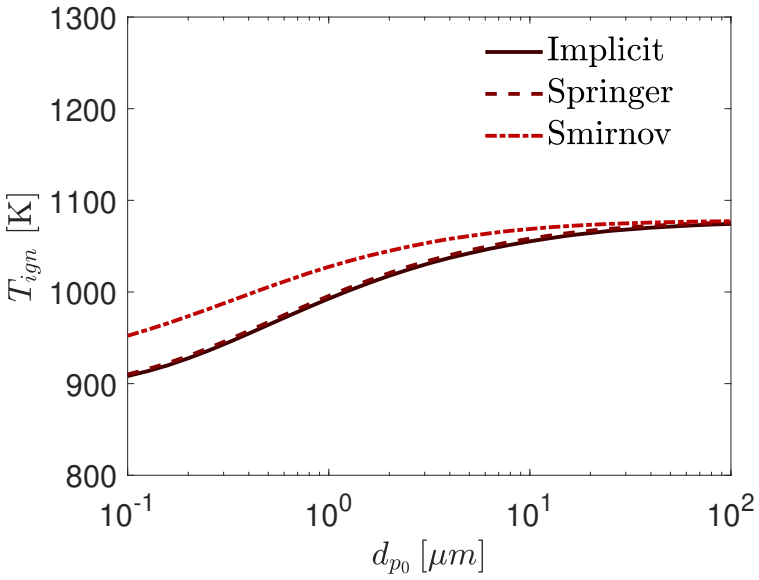

Figure 5.2: Ignition temperature as a function of particle size with an initial oxide layer thickness of 1 nm with the different numerical solution methods.

three methods are in excellent agreement across the entire range of particle sizes considered, which map an initial Knudsen number between 1.57 x 10^{-3} and 1.37 at the ignition temperature. If the fully implicit boundary method is considered to be the exact solution, the Springer and Smirnov formulations predict ignition temperatures in agreement to within $\approx$ 0.3% and 5%, respectively, or within 3 K to 50 K. Since the Springer formulation is the boundary sphere method with an assumption of small temperature difference between the bulk gas and the particle, its results are practically identical to the implicit formulation, which verifies this assumption for the ignition problem. Unless otherwise stated, the remainder of the results presented in the current chapter are based on the Springer formulation, as it requires a third of the computational cost of the implicit formulation.

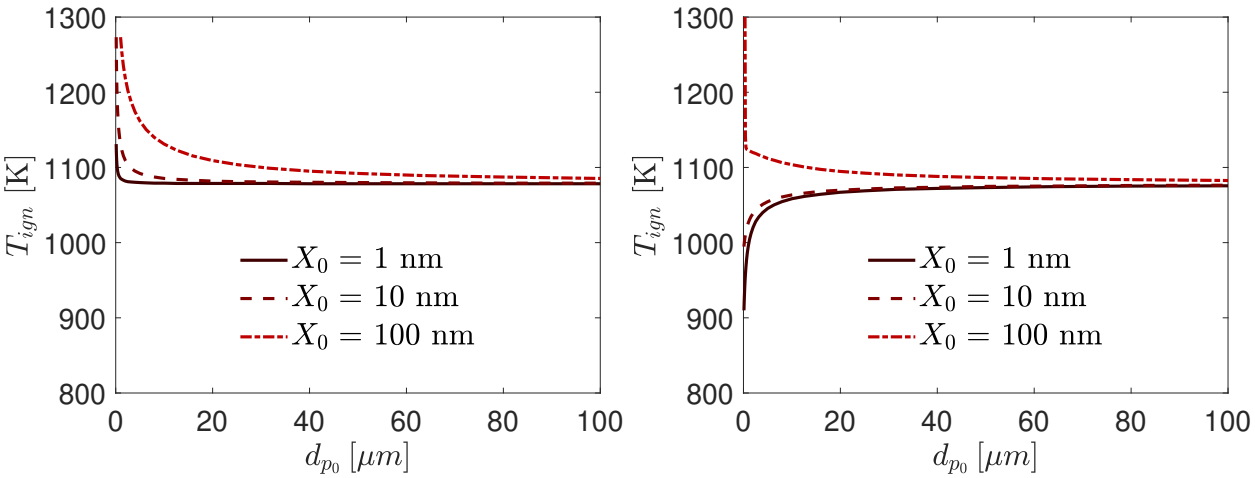

(a) Continuum approximation.

(b) Boundary sphere method.

Figure 5.3: Ignition temperature as a function of initial particle size for different initial oxide layer thicknesses.

5.2 Ignition Behavior

5.2.1 Effect of Particle Size and Oxide Layer Thickness

Figure 5.3 shows the ignition temperature as a function of particle size for different initial total oxide layer thicknesses, for the continuum (Figure 5.3a) and boundary sphere (Figure 5.3b) solutions. Figure 5.3a is in perfect agreement with the results obtained by Mi et al. [3], which were based on a continuum analysis. Figure 5.3b shows that at large particle sizes, the Knudsen transition effects become negligible, and the boundary sphere method recovers the continuum solution: an independence of the ignition temperature from the particle size, as shown by the plateauing curves. However, opposite trends of the ignition temperatures for $X_0 = 1$ nm and $X_0 = 10$ nm are predicted by the two different methods. The continuum approximation shows an increase of the ignition temperature with decreasing particle size, whereas the boundary sphere method predicts the opposite trend. For the X_0 = 100 nm curve, the boundary sphere method predicts an increase of the ignition temperature with decreasing particle size, but the asymptotic behavior of the curve is observed at a lower particle size than with the continuum approximation.

The trends observed in Figure 5.3b can be explained by considering the theory behind transition and free-molecular transport and solid-phase iron oxidation. As the particle size is being decreased to a size comparable to the mean free path of the gas molecules, the molecule-particle collision rate decreases. Since the iron reaction is independent on the delivery rate of oxidizer to the particle surface in the kinetic-limited regime (i.e. for the majority of the period before thermal runaway occurs), the internal reaction rates are not affected by the decaying molecule-particle collision rate. However, the heat loss rate from the particle decreases, as the collisions from the gas molecules that can carry heat away from it are reduced. This results in a net thermal insulating effect on the particle, which leads to an easier ability to ignite for smaller particles, as observed for the X_0 = 1 nm and X_0 = 10 nm curves. As well, the curve X_0 = 10 nm leads to higher ignition temperatures than the curve X_0 = 1 nm: thickening the oxide layer on the particle surface has the effect of decelerating the reaction kinetics, as the iron and oxygen ions must diffuse through a larger lattice before they can react at the interfaces. As well, the thicker oxide layer means more thermal mass must be heated by the particle reaction before thermal runaway and ignition can occur. In the case X_0 = 100 nm, these adverse effects of the oxide layer on the ignition of the particle are further pronounced. Additionally, as the particle size is being decreased while maintaining a constant initial oxide layer thickness, the proportion of available Fe content to react and release heat is reduced. For sufficiently thick oxide layers (e.g. X_0 = 100 nm), this effect outweighs the thermal insulating effect of the transition transport regime, and the net result is an increase in ignition temperature with decreasing particle size. The asymptotic behavior is nevertheless observed at a much lower particle size than with the continuum solution, as can be seen from Figure 5.3.

To further assess the ignition behavior as a function of particle size at different oxide layer thicknesses, Figure 5.4 shows the results on a semi-logarithmic plot. Although at first glance Figure 5.3b seems to predict that the ignition temperature decays continuously as the particle size is being decreased for the X_0 = 1 nm and X_0 = 10 nm curves, Figure 5.4 shows the curves go through an inflexion point and tend towards a plateau in the small particle limit. Sufficiently decreasing the Fe content (i.e., further reducing the particle size) would then eventually lead to asymptotic behavior of the ignition temperature, as observed with the X_0 = 100 nm curve.

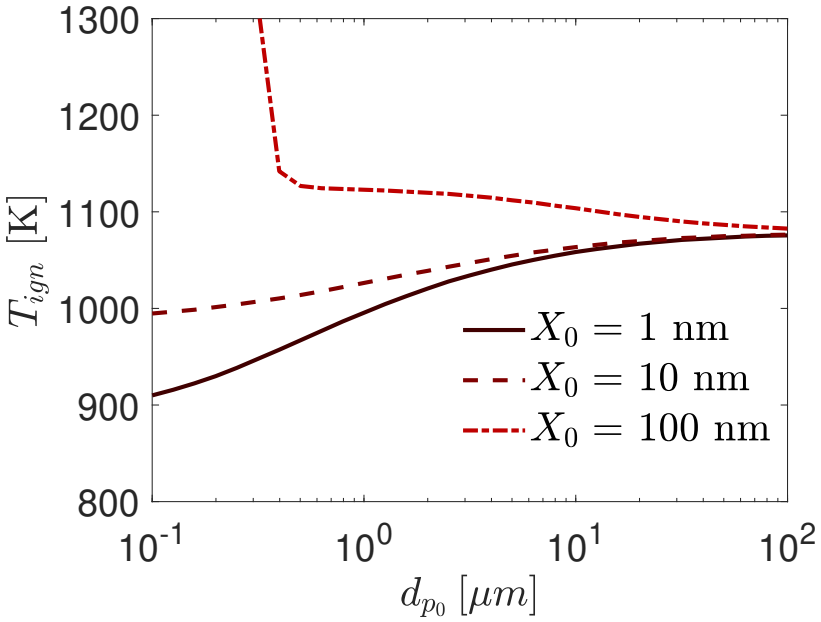

Figure 5.4: Ignition temperature as a function of initial particle size with the boundary sphere method on a semi-logarithmic plot.

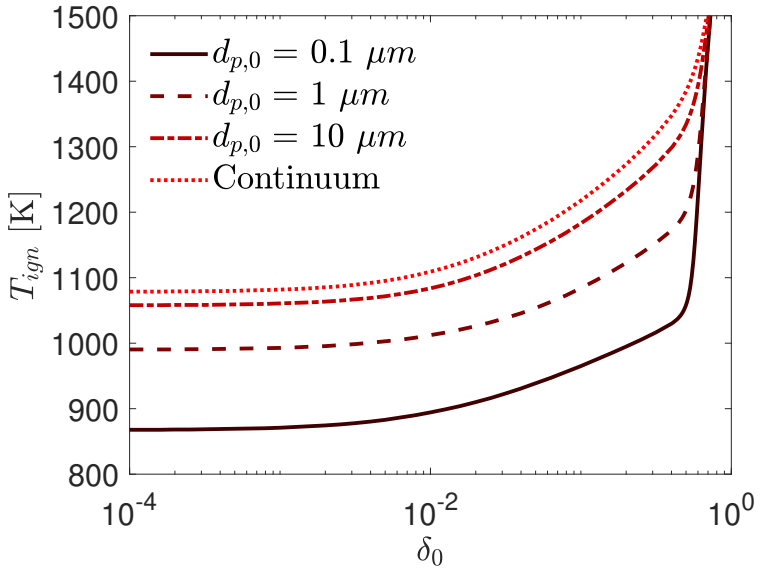

Figure 5.5: Ignition temperature as a function of initial oxide thickness ratio for different particle sizes. Continuum curve: independence of the ignition temperature on particle size. Boundary sphere method: dependence on both the particle size and the initial oxide thickness ratio.

An additional assessment of the effect of the oxide layer thickness can be obtained by considering the ratio of initial oxide layer thickness to the total particle size δ_0, as defined by Equation 4.37. Figure 5.5 shows the ignition temperature as a function of δ_0 for different particle sizes as resolved by the boundary sphere method, and once for the continuum result. The ignition temperature is independent on particle size at constant δ_0 in the continuum limit, hence a single curve is displayed. The qualitative trends of the curves are identical independent of particle size: at low δ_0, a plateau is observed. As the ratio of initial oxide layer thickness to particle size tends to 0, the decelerating kinetics and increased inert thermal mass to heat from the oxide layer become negligible, and the ignition temperature is solely governed by the particle initial size, which governs the heat loss rate. As δ_0 increases, the ignition temperature increases, as a result of the decelerating kinetics from the oxide lattice diffusion and the inert thermal mass. As δ_0 tends to 1, the ignition temperature tends to infinity: the lattice diffusion largely inhibits the reaction rate of the particles, and the inert thermal mass becomes too large relative to the size of the particle. There is insufficient Fe content to initiate ignition.

5.2.2 Ignition Criterion

To understand how the ignition temperature changes with particle size, a simple steady-state Semenov analysis can be performed, neglecting the oxide scale growth on the particle surface as well as the enthalpy increase of the particle related to incorporation of O_2. Ignition occurs when the heat generation rate exceeds the heat loss rate, hence when $\dot{Q}_\mathrm{R} > \dot{Q}_\mathrm{p}$. The heat generation rate is given by [3]:

$$\dot{Q}_\mathrm{R} = \left[\bar{q}\exp\left(\frac{-T_\mathrm{a}}{T_\mathrm{p}}\right)\right]\Bigg|_{\mathrm{FeO}} \frac{(1-\delta\delta_{\mathrm{Fe_3O_4}})^2 r_\mathrm{p}}{\delta - \delta\delta_{\mathrm{Fe_3O_4}}} + \left[\bar{q}\exp\left(\frac{-T_\mathrm{a}}{T_\mathrm{p}}\right)\right]\Bigg|_{\mathrm{Fe_3O_4}} \frac{r_\mathrm{p}}{\delta\delta_{\mathrm{Fe_3O_4}}} \tag{5.1}$$

where $\bar{q}_i = \rho_i q_i k_{0,i}$, with ρ_i the density of the ith oxide, q_i its heating value, and $k_{0,i}$ its pre-exponential Arrhenius constant. At constant δ, the heat release rate scales with r_p. Using Equation 4.46, and substituting the Knudsen number by its definition $\mathrm{Kn} = \lambda_{\mathrm{MFP,g}}/r_\mathrm{p} \equiv \theta/r_\mathrm{p}$, the heat loss

rate can be written as:

$$\dot{Q}_{\mathrm{p}} = 8\pi r_{\mathrm{p}}^2 k_{\mathrm{g}}(T_{\mathrm{p}} - T_{\mathrm{g}})\left(\frac{r_{\mathrm{p}} + \theta}{2r_{\mathrm{p}}^2 + G\theta r_{\mathrm{p}} + G\theta^2}\right) \tag{5.2}$$

where $G = \frac{2(9\gamma-5)}{\alpha_{\mathrm{T}}(\gamma+1)}$. Note this formulation incorporates the assumption of small temperature difference, as well as the approximation $\theta = \lambda_{\mathrm{MFP,g}}$. It is valid for the entire range of Knudsen number.

In the continuum limit, $r_{\mathrm{p}} >> \theta$, in which case $r_{\mathrm{p}} + \theta \rightarrow r_{\mathrm{p}}$, and $2r_{\mathrm{p}}^2 + G\theta r_{\mathrm{p}} + G\theta^2 \rightarrow 2r_{\mathrm{p}}^2$. Equation 5.2 then yields $\dot{Q}_{\mathrm{p}} \rightarrow 4\pi k_{\mathrm{g}}(T_{\mathrm{p}} - T_{\mathrm{g}})r_{\mathrm{p}}$, which is identical to the heat loss rate in the continuum regime. Then the ignition criterion becomes:

$$\left[\bar{q}\exp\left(\frac{-T_{\mathrm{a}}}{T_{\mathrm{p}}}\right)\right]\Bigg|_{\mathrm{FeO}} \frac{(1-\delta\delta_{\mathrm{Fe_3O_4}})^2 r_{\mathrm{p}}}{\delta - \delta\delta_{\mathrm{Fe_3O_4}}} + \left[\bar{q}\exp\left(\frac{-T_{\mathrm{a}}}{T_{\mathrm{p}}}\right)\right]\Bigg|_{\mathrm{Fe_3O_4}} \frac{r_{\mathrm{p}}}{\delta\delta_{\mathrm{Fe_3O_4}}} > 4\pi k_{\mathrm{g}}(T_{\mathrm{p}} - T_{\mathrm{g}})r_{\mathrm{p}}. \tag{5.3}$$

At constant δ, both sides of Equation 5.3 scale with r_{p}. This leads to the independence of the ignition temperature on particle size in the continuum limit, i.e. at large particle size, as observed by the plateau in Figure 5.6a.

In the free-molecular limit, $\theta >> r_{\mathrm{p}}$, and $r_{\mathrm{p}} + \theta \rightarrow \theta$. As well, $2r_{\mathrm{p}}^2 + G\theta r_{\mathrm{p}} + G\theta^2 \rightarrow G\theta^2$. Equation 5.2 then yields $\dot{Q}_{\mathrm{p}} \rightarrow 8\pi r_{\mathrm{p}}^2 k_{\mathrm{g}}(T_{\mathrm{p}} - T_{\mathrm{g}})/(G\theta)$. Then the ignition criterion becomes:

$$\left[\bar{q}\exp\left(\frac{-T_{\mathrm{a}}}{T_{\mathrm{p}}}\right)\right]\Bigg|_{\mathrm{FeO}} \frac{(1-\delta\delta_{\mathrm{Fe_3O_4}})^2 r_{\mathrm{p}}}{\delta - \delta\delta_{\mathrm{Fe_3O_4}}} + \left[\bar{q}\exp\left(\frac{-T_{\mathrm{a}}}{T_{\mathrm{p}}}\right)\right]\Bigg|_{\mathrm{Fe_3O_4}} \frac{r_{\mathrm{p}}}{\delta\delta_{\mathrm{Fe_3O_4}}} > \frac{8\pi r_{\mathrm{p}}^2 k_{\mathrm{g}}}{G\theta}(T_{\mathrm{p}} - T_{\mathrm{g}}) \tag{5.4}$$

which shows the heat loss rate scales with r_{p}^2, whereas the heat generation rate scales with r_{p}. Hence in the free-molecular limit, at constant δ, if the particle size increases, the ignition temperature increases, since the heat loss rate increases faster than the heat generation rate. This explains the decaying trend of the ignition temperature at constant δ_0, as shown in Figure 5.6b.

It should be noted that the current model predicts a continuous decay of the ignition temperature with decreasing particle size. However, the iron particle kinetics are well-defined only in the temperature range 973 K to 1573 K, as stated in Section 2.2.1, while the lowest ignition temperature

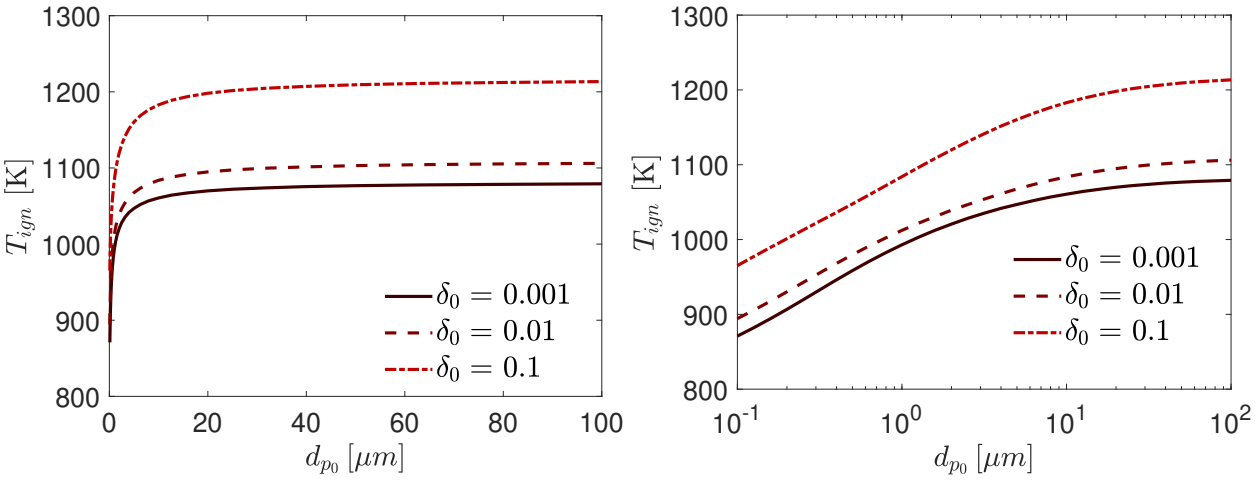

(a) Regular x-axis showing the plateau in the large particle limit.

(b) Semi-logarithmic plot showing the decay with $d_{\mathrm{p},0}$ in the small particle limit.

Figure 5.6: Ignition temperature as a function of initial particle size for different initial oxide layer thickness ratios δ_0.

predicted by Figure 5.6 is around 870 K. Hence, the iron kinetics are extended around 100 K below their confidence interval in the current analysis. To provide an accurate qualitative and quantitative description of the ignition behavior at smaller particle sizes, a different kinetic formulation for iron oxidation is required. It is hypothesized that the different oxidation kinetics would eventually lead to a plateau in ignition temperature for smaller particles.

5.3 Continuum Approximation Limit

Figure 5.7 shows the ratio of the ignition temperature predicted by the boundary sphere method to the ignition temperature predicted by the continuum approximation as a function of particle size, as well as the difference between these two quantities. As expected, $T_{\mathrm{ign}}/T_{\mathrm{ign,co}} \rightarrow 1$ as the particle size is being increased, which validates the use of continuum modeling to describe transport processes at large particle sizes. At $\delta_0 = 0.10$, the continuum approximation is accurate to within 90% for initial particle diameters exceeding $\approx 1\,\mu$m, and to within 95% for particles exceeding $\approx 5\,\mu$m, which corresponds to temperature differences in the vicinity of 50 K - 100 K. In practice, such small temperature differences on ignition temperatures neighbouring 1000 K

cannot be resolved by experimental measurements. At ≈ 40 μm, the continuum results are above 99% accurate or within 10 K. In reality, practical iron burner applications would use powders composed of particles of several tens or hundreds of microns. Continuum transport is therefore largely sufficient to eventually model such systems.

5.4 Comparison with Literature

Senyurt & Dreizin [18] conducted an analysis of the effect of the Knudsen transition regime on the ignition behavior of aluminum, magnesium, and boron particles. They proposed kinetic formulations for the different metals which do not consider oxide layer growth on the particle surface and derived ignition temperatures using a steady state analysis with the boundary sphere method. The authors concluded that the Knudsen transition regime effects must be accounted for particles as large as 200 μm in modeling efforts. As well, they predicted that the ignition temperature always increases with decreasing particle size. These conclusions are analyzed in the current section.

The proposed formulation by Senyurt & Dreizin [18] for the heat release rate from the particles considers simple kinetics:

$$\dot{Q}_{\mathrm{R}} = q A_{\mathrm{p}} C_{\mathrm{O_2,p}} \dot{\omega} \tag{5.5}$$

where q is the gravimetric heat of oxidation, $A_{\mathrm{p}} = 4\pi r_{\mathrm{p}}^2$ is the particle surface area, $C_{\mathrm{O_2,p}}$ is the oxidizer concentration at the particle surface, and $\dot{\omega} = K \exp(-T_{\mathrm{a}}/T_{\mathrm{p}})$ is the regression rate of the fuel particle surface, with K a pre-exponential rate constant, T_{a} an activation temperature, and T_{p} the particle temperature. Multiple different formulations for K are proposed depending on the

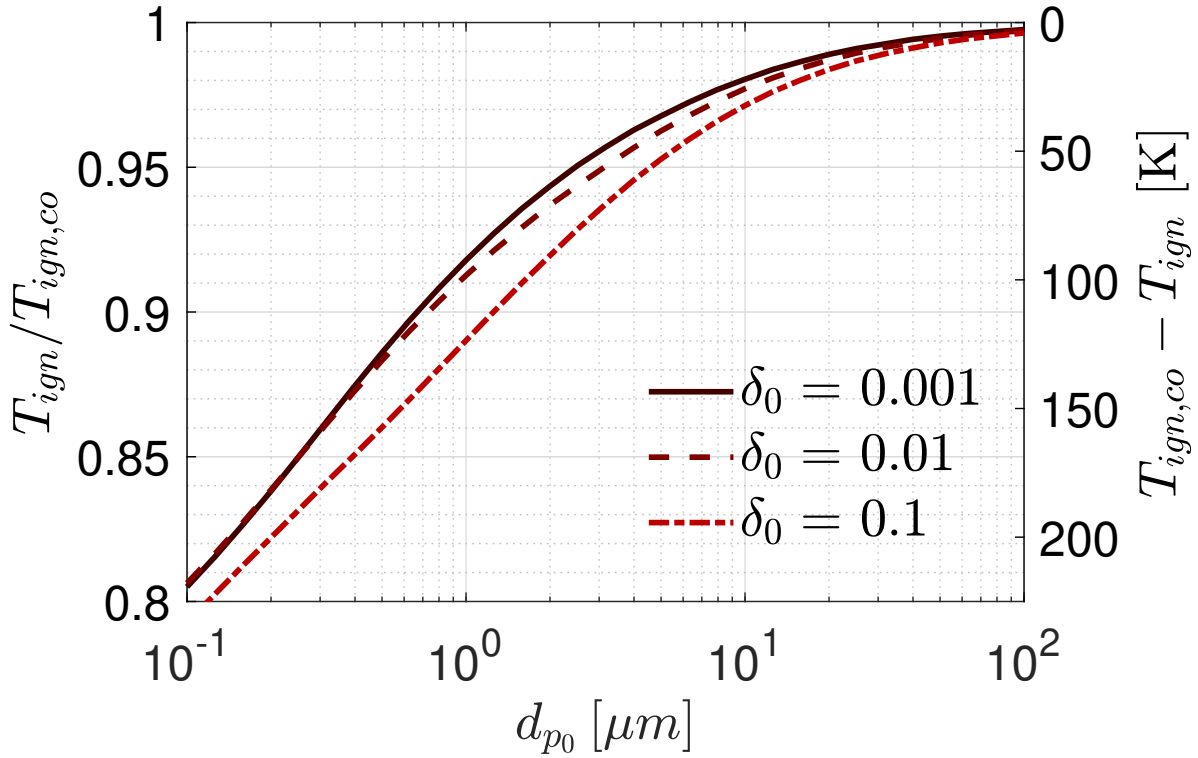

(a) Comparison on a semi-logarithmic plot.

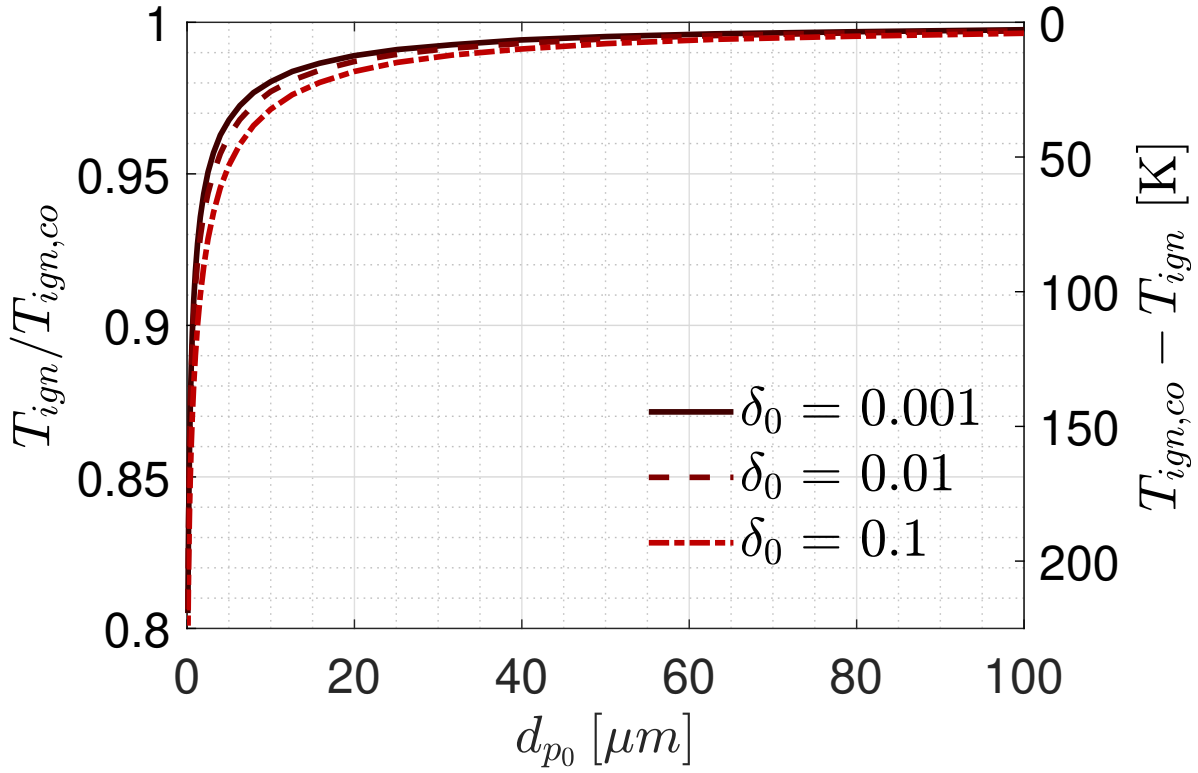

(b) Comparison on a regular plot.

Figure 5.7: Comparison of the ignition temperatures computed by the boundary sphere result T_{ign} and those computed by the continuum result $T_{\text{ign,co}}$.

kinetic model of the specific metal:

$$K = \frac{K_1}{C_{\mathrm{O_2,p}}} \tag{5.6}$$

$$K = \frac{K_2}{X_{\text{oxide}} C_{\mathrm{O_2,p}}} \frac{\rho_{\text{oxide}}}{\nu_{\text{oxide}}} \tag{5.7}$$

$$K = \frac{K_3}{C_{\mathrm{O_2,p}}} p_{\mathrm{O_2,p}} \tag{5.8}$$

$$K = \frac{K_4}{\nu C_{\mathrm{O_2,p}}} \frac{m_{pp}}{A_{pp}}. \tag{5.9}$$

The parameters defined are: K_i a rate constant; X_{oxide} an initial oxide layer thickness; ρ_{oxide} the oxide layer mass density; ν_{oxide} the stoichiometric mass ratio relating the oxide layer mass to the fuel mass; $p_{\mathrm{O_2,p}}$ the partial pressure of oxygen; $m_{\mathrm{p,p}}$ the agglomerated mass of particles; and A_{pp} the agglomeration surface area. In Equation 5.7, it is very important to note that X_{oxide} is formulated as an initial oxide layer thickness, but the model implementation by Senyurt & Dreizin does not consider the transient oxide layer growth. Instead, X_{oxide} is assumed to be a constant, and so it simply constitutes a parameter like any other, and the kinetic model does not have the features of the parabolic kinetic model formulated in the current work.

In general, Equations 5.6 to 5.9 take the following form:

$$K = \frac{K_i(\mathbf{y})}{C_{\mathrm{O_2,p}}} \tag{5.10}$$

where $K_i(\mathbf{y})$ is a constant defined from multiple parameters $\mathbf{y}$ that vary from one kinetic formulation to another. Using Equation 5.5, the heat release rate from the particle is then:

$$\dot{Q}_{\mathrm{R}} = 4\pi r_{\mathrm{p}}^2 q K_i(\mathbf{y}) \exp\left(\frac{-T_{\mathrm{a}}}{T_{\mathrm{p}}}\right). \tag{5.11}$$

Using Equation 5.2 and considering the continuum limit (large r_{p}) the ignition criterion can then be written as:

$$4\pi r_{\mathrm{p}}^2 q K_i(\mathbf{y}) \exp\left(\frac{-T_{\mathrm{a}}}{T_{\mathrm{p}}}\right) > 4\pi r_{\mathrm{p}} k_{\mathrm{g}} (T_{\mathrm{p}} - T_{\mathrm{g}}). \tag{5.12}$$

The heat release rate scales with r_{p}^2, whereas the heat loss rate scales with r_{p}. Hence towards the continuum limit, the ignition temperature decreases as the particle size increases, since the heat release rate increases faster than the heat loss rate. This is indeed the results obtained by the authors, who always predicted a decrease of the ignition temperature with increasing particle size. This is also in agreement with the first-order kinetics considered by Soo et al. [2], a first-order kinetics continuum model. Conversely, in the free-molecular limit, the ignition criterion becomes:

$$4\pi r_{\mathrm{p}}^2 q K_i(\mathbf{y}) \exp\left(\frac{-T_{\mathrm{a}}}{T_{\mathrm{p}}}\right) > \frac{8\pi r_{\mathrm{p}}^2 k_{\mathrm{g}}}{G\theta}(T_{\mathrm{p}} - T_{\mathrm{g}}). \tag{5.13}$$

In this limit, both sides of Equation 5.13 scale with r_{p}^2, and so the ignition criterion becomes independent of particle size, but is only a function of the kinetic and transport parameters postulated in the model. Senyurt & Dreizin performed a parametric study of the impact of the thermal accommodation coefficient α_{T} on the ignition temperature in their work. It is shown that at small α_{T}, i.e. when transition transport effects become increasingly important, the ignition temperature plateaus for all the kinetic formulations towards the small particle limit. This is in agreement with Equation 5.13, which postulates that the ignition temperature is independent of particle size towards the free-molecular limit.

In the current work, the left-hand-side of Equation 5.4 only scales with r_{p} at constant δ in the parabolic kinetic formulation in the free-molecular limit. This is what leads to the opposite predicted trend, by which the ignition temperature always decreases with decreasing particle size as shown in Figure 5.6b, whereas Senyurt & Dreizin predicted the ignition temperature always increases with decreasing particle size. The analysis presented in this section therefore reconcile the results obtained from the current work with those obtained by Senyurt & Dreizin.

Additionally, the authors claimed that transition modeling must be accounted for particle sizes up to 200 μm. The authors performed parametric studies on the metals with α_{T} ranging from 0.01 to 1. It should be noted that at 200 μm particle size, the difference between the continuum and boundary sphere results presented by the author as predicted with $\alpha_{\mathrm{T}} = 0.01$ is within $\approx$ 50 K, on ignition temperatures ranging from the high hundreds to the thousands of Kelvins. In experimen-

tal applications, the accuracy of measurement techniques can hardly resolve such a precision. As well, this constitutes a negligible error, considering the relative simplicity of continuum modeling when compared to transition transport modeling. These strong claims by the authors for establishing the importance of transition effects for particles up to 200 μm are therefore unfounded. The current work confirms that, as reported by a majority of previous authors [13, 16, 17], transition transport effects become important for particles in the low tens of microns and for nanoparticles at atmospheric pressure.

5.5 Concluding Remarks

The current study aimed to quantitatively assess Knudsen transition transport effects on the ignition behavior of fine iron particles. The analysis also aimed to characterize a threshold of particle size above which transition transport effects could be neglected for iron ignition problems. A computational program combining a parabolic kinetic formulation for iron oxidation with oxide layer growth, and a boundary sphere transition transport model was implemented. The thermal insulating effect of the transition transport was shown to lead to a decrease in ignition temperature with decreasing particle size at constant initial oxide layer thickness ratio in the free-molecular limit. In the continuum limit, the ignition temperature was shown to be independent of particle size and only a function of the initial oxide layer thickness ratio. The inhibiting effect of large oxide layers was shown to lead to an asymptotic behavior of the ignition temperature as the oxide layer thickness ratio tended to 1. Continuum transport modeling was shown to accurately predict ignition temperatures to within 5% error for particles exceeding 5 μm initial diameter, and to within 1% error for particles exceeding 40 μm, or within 10-50 K. These errors are negligible for ignition temperatures neighbouring 1000 K. The current work confirmed that, as reported by the majority of previous authors considering heterogeneous reaction problems, transition transport effects become important for particles sizes in the low tens of microns and for nanoparticles. The controversial claim by Senyurt & Dreizin [18] of these effects being important at sizes up to 200 μm was shown to be unfounded. As practical iron burner applications would eventually rely on

particles in the tens of microns or several hundreds of microns in diameter, continuum transport modeling is largely sufficient to predict the ignition behavior of such large particles.

In future modeling efforts, a better quantitative assessment of the ignition temperature of iron particles below $\approx$ 50 nm should be anchored in a kinetic iron oxidation formulation experimentally validated for temperature ranges below 973 K. As well, the thermal accommodation coefficient should be better characterized to reduce the width of the confidence interval 0.08-0.90. Additionally, transition transport effects could be investigated on the ignition behavior of suspensions of iron microparticles, as an extension to the isolated iron particle ignition problem.

Bibliography

[1] J. M. Bergthorson, "Recyclable metal fuels for clean and compact zero-carbon power," *Progress in Energy and Combustion Science*, vol. 68, pp. 169–196, 2018.

[2] M. Soo, X. Mi, S. Goroshin, A. J. Higgins, and J. M. Bergthorson, "Combustion of particles, agglomerates, and suspensions–a basic thermophysical analysis," *Combustion and Flame*, vol. 192, pp. 384–400, 2018.

[3] X. Mi, A. Fujinawa, and J. M. Bergthorson, "A quantitative analysis of the ignition characteristics of fine iron particles," 2021.

[4] J. Bergthorson, S. Goroshin, M. Soo, P. Julien, J. Palecka, D. Frost, and D. Jarvis, "Direct combustion of recyclable metal fuels for zero-carbon heat and power," *Applied Energy*, vol. 160, pp. 368–382, 2015.

[5] T. M. Letcher, "Climate change: observed impacts on planet earth," 2009.

[6] ——, "The impacts of climate change: A comprehensive study of physical, biophysical, social, and political issues," 2021.

[7] D. A. Frank-Kamenetskii, *Diffusion and heat exchange in chemical kinetics*. Princeton University Press, 1955.

[8] B. Khaikin, V. Bloshenko, and A. G. Merzhanov, "On the ignition of metal particles," *Combustion, Explosion and Shock Waves*, vol. 6, no. 4, pp. 412–422, 1970.

[9] D. Meinköhn, "The effect of particle size and ambient oxidizer concentration on metal particle ignition," *Combustion science and technology*, vol. 181, no. 8, pp. 1007–1037, 2009.

[10] J. Benard, "The oxidation of metals and alloys," *Metallurgical Reviews*, vol. 9, no. 1, pp. 473–503, 1964.

[11] K. R. Lawless, "The oxidation of metals," *Reports on Progress in Physics*, vol. 37, no. 2, p. 231, 1974.

[12] A. Merzhanov, "Thermal theory of metal particle ignition," *AIAA Journal*, vol. 13, no. 2, pp. 209–214, 1975.

[13] R. Gopalakrishnan, T. Thajudeen, and C. J. Hogan Jr, "Collision limited reaction rates for arbitrarily shaped particles across the entire diffusive knudsen number range," *The Journal of chemical physics*, vol. 135, no. 5, p. 054302, 2011.

[14] T. T. Kodas and P. B. Comita, "The role of mass transport in laser-induced chemistry," *Accounts of Chemical Research*, vol. 23, no. 6, pp. 188–194, 1990.

[15] F. Liu, K. Daun, D. R. Snelling, and G. J. Smallwood, "Heat conduction from a spherical nano-particle: status of modeling heat conduction in laser-induced incandescence," *Applied physics B*, vol. 83, no. 3, pp. 355–382, 2006.

[16] A. Shpara, D. Yagodnikov, and A. Sukhov, "Effect of particle size on boron combustion in air," *Combustion, Explosion, and Shock Waves*, vol. 56, no. 4, pp. 471–478, 2020.

[17] S. Mohan, M. A. Trunov, and E. L. Dreizin, "Heating and ignition of metal particles in the transition heat transfer regime," 2008.

[18] E. I. Senyurt and E. L. Dreizin, "At what ambient temperature can thermal runaway of a burning metal particle occur?" *Combustion and Flame*, vol. 236, p. 111800, 2022.

[19] R. B. Bird, W. E. Stewart, and E. N. Lightfoot, *Transport phenomena*. John Wiley & Sons, 2006, vol. 1.

[20] S. Whitaker, "Forced convection heat transfer correlations for flow in pipes, past flat plates, single cylinders, single spheres, and for flow in packed beds and tube bundles," *AIChE Journal*, vol. 18, no. 2, pp. 361–371, 1972.

[21] L. A. Vulis, *Thermal regimes of combustion*. McGraw-Hill, 1961.

[22] J. Païdassi, "Sur la cinetique de l'oxydation du fer dans l'air dans l'intervalle 700–1250° c," *Acta Metallurgica*, vol. 6, no. 3, pp. 184–194, 1958.

[23] A. G. Goursat and W. Smeltzer, "Kinetics and morphological development of the oxide scale on iron at high temperatures in oxygen at low pressure," *Oxidation of Metals*, vol. 6, no. 2, pp. 101–116, 1973.

[24] S. Chapman and T. G. Cowling, *The mathematical theory of non-uniform gases: an account of the kinetic theory of viscosity, thermal conduction and diffusion in gases*. Cambridge university press, 1990.

[25] E. H. Kennard, *Kinetic Theory of Gases, With an Introduction to Statistical Mechanics*. McGraw-Hill, New York, 1938.

[26] B. McCoy and C. Cha, "Transport phenomena in the rarefied gas transition regime," *Chemical Engineering Science*, vol. 29, no. 2, pp. 381–388, 1974.

[27] W. Arabczyk and U. Narkiewicz, "Interpretation of kinetics of iron surface oxidation involving the real structure of single crystal samples," *Czechoslovak Journal of Physics*, vol. 43, no. 9, pp. 869–873, 1993.

[28] C. F. Brucker and T. N. Rhodin, "Oxygen chemisorption and reaction on α-fe (100) using photoemission and low-energy electron diffraction," *Surface Science*, vol. 57, no. 2, pp. 523–539, 1976.

[29] C. Brundle, "Oxygen adsorption and thin oxide formation at iron surfaces: An xps/ups study," *Surface Science*, vol. 66, no. 2, pp. 581–595, 1977.

[30] G. W. Simmons and D. J. Dwyer, "A leed-aes study of the initial stages of oxidation of fe (001)," *Surface Science*, vol. 48, no. 2, pp. 373–392, 1975.

[31] T. Smith, "Effect of surface coverage and temperature on the sticking coefficient," *The Journal of Chemical Physics*, vol. 40, no. 7, pp. 1805–1812, 1964.

[32] F. O. Goodman, "Thermal accommodation," *Progress in Surface Science*, vol. 5, pp. 261–375, 1974.

[33] S. Song and M. Yovanovich, "Correlation of thermal accommodation coefficient for engineering surfaces," *ASME HTD*, vol. 69, pp. 107–116, 1987.

[34] L. B. Thomas, "Thermal accommodation of gases on solids," in *Fundamentals of Gas–Surface Interactions*. Elsevier, 1967, pp. 346–369.

[35] H. Y. Wachman, "The thermal accommodation coefficient: a critical survey," *ARS Journal*, vol. 32, no. 1, pp. 2–12, 1962.

[36] N. A. Fuchs, *Evaporation and droplet growth in gaseous media*. Elsevier, 1959.

[37] E. Fuller and J. Giddings, "A comparison of methods for predicting gaseous diffusion coefficients," *Journal of Chromatographic Science*, vol. 3, no. 7, pp. 222–227, 1965.

[38] P. E. Wagner, "Aerosol growth by condensation," in *Aerosol Microphysics II*. Springer, 1982, pp. 129–178.

[39] D. W. Green and R. H. Perry, *Perry's chemical engineers' handbook*. McGraw-Hill Education, 2008.

[40] B. J. McBride, *Coefficients for calculating thermodynamic and transport properties of individual species*. NASA Langley Research Center, 1993, vol. 4513.

[41] P. Wright, "On the discontinuity involved in diffusion across an interface (the δ of fuchs)," *Discussions of the Faraday Society*, vol. 30, pp. 100–112, 1960.

[42] M. Smoluchowski von Smolan, "Ueber wärmeleitung in verdünnten gasen," *Annalen der Physik*, vol. 300, no. 1, pp. 101–130, 1898.

[43] R. Bradley, M. G. Evans, and R. Whytlaw-Gray, "The rate of evaporation of droplets. evaporation and diffusion coefficients, and vapour pressures of dibutyl phthalate and butyl stearate," *Proceedings of the Royal Society of London. Series A. Mathematical and Physical Sciences*, vol. 186, no. 1006, pp. 368–390, 1946.

[44] I. Langmuir, "The dissociation of hydrogen into atoms.[part ii.] calculation of the degree of dissociation and the heat of formation." *Journal of the American Chemical Society*, vol. 37, no. 3, pp. 417–458, 1915.

[45] G. S. Springer and S. W. Tsai, "Method for calculating heat conduction from spheres in rarefied gases," *The Physics of Fluids*, vol. 8, no. 8, pp. 1561–1563, 1965.

[46] P. L. Bhatnagar, E. P. Gross, and M. Krook, "A model for collision processes in gases. i. small amplitude processes in charged and neutral one-component systems," *Physical review*, vol. 94, no. 3, p. 511, 1954.

[47] M. Chase, *NIST-JANAF Thermochemical Tables, 4th Edition*. American Institute of Physics, -1, 1991.

[48] G. Hubbard, V. Denny, and A. Mills, "Droplet evaporation: effects of transients and variable properties," *International journal of heat and mass transfer*, vol. 18, no. 9, pp. 1003–1008, 1975.

[49] E. N. Fuller, P. D. Schettler, and J. C. Giddings, "New method for prediction of binary gas-phase diffusion coefficients," *Industrial & Engineering Chemistry*, vol. 58, no. 5, pp. 18–27, 1966.

[50] K. Daun, T. Sipkens, J. Titantah, and M. Karttunen, "Thermal accommodation coefficients for laser-induced incandescence sizing of metal nanoparticles in monatomic gases," *Applied Physics B*, vol. 112, no. 3, pp. 409–420, 2013.

[51] T. Sipkens, N. Singh, K. Daun, N. Bizmark, M. Ioannidis, J. Titantah, and M. Karttunen, "Time resolved laser induced incandescence for sizing aerosolized iron nanoparticles," in *ASME International Mechanical Engineering Congress and Exposition*, vol. 46569. American Society of Mechanical Engineers, 2014, p. V08BT10A051.

[52] T. Sipkens, N. Singh, K. Daun, N. Bizmark, and M. Ioannidis, "Examination of the thermal accommodation coefficient used in the sizing of iron nanoparticles by time-resolved laser-induced incandescence," *Applied Physics B*, vol. 119, no. 4, pp. 561–575, 2015.

[53] T. Sipkens, K. Daun, J. Titantah, and M. Karttunen, "Quantifying the thermal accommodation coefficient for iron surfaces using molecular dynamics simulations," in *ASME International Mechanical Engineering Congress and Exposition*, vol. 57502. American Society of Mechanical Engineers, 2015, p. V08BT10A027.

[54] T. Sipkens and K. Daun, "Effect of surface interatomic potential on thermal accommodation coefficients derived from molecular dynamics," *The Journal of Physical Chemistry C*, vol. 122, no. 35, pp. 20 431–20 443, 2018.

Appendix A

Thermophysical and Transport Properties

A.1 Shomate Polynomials

The Shomate polynomials for thermophysical properties of condensed-phase species are formulated as follows [47]:

$$\begin{aligned} t &= T/1000 \\ c_p\,[\text{J/(mol.K)}] &= A + Bt + Ct^2 + Dt^3 + \frac{E}{t^2} \\ h\,[\text{kJ/mol}] &= At + \frac{Bt^2}{2} + \frac{Ct^3}{3} + \frac{Dt^4}{4} - \frac{E}{t} + F - H \end{aligned}$$

where T is the temperature in Kelvins, c_p is the molar heat capacity at constant pressure, and h is the molar enthalpy. They are converted to gravimetric values using the molar weight of the species. In their study, Mi et al. [3] adjusted the H constants of Fe to remove small discontinuities of the Shomate polynomials at bounds between temperature intervals. The H constants used for Fe in the current work are those provided by Mi et al. The constants for the different species and the temperature ranges are shown in Tables A.1 to A.3 for temperatures below the melting point of the species.

Table A.1: Shomate constants for iron (Fe) in the α phase.

Range [K]	298-700	700-1042	1042-1100	1100-1809
A	18.42868	-57767.65	-325.8859	-776.7387
B	24.64301	137919.7	28.92876	919.4005
C	-8.913720	-122773.2	0	-383.7184
D	9.664706	38682.42	0	57.08148
E	-0.012643	3993.08	411.9629	242.1369
F	-6.573022	24078.67	745.8231	697.6234
H	0	141E-03	-71E-03	-436E-03

Table A.2: Shomate constants for wüstite (FeO).

Range [K]	298-1650
A	45.75120
B	18.78553
C	-5.952201
D	0.852779
E	-0.081265
F	-286.7429
H	-272.0441

Table A.3: Shomate constants for magnetite (Fe_3O_4).

Range [K]	298-900	900-1811
A	104.2096	200.8320
B	178.5108	1.586435E-07
C	10.6151	-6.661682E-08
D	1.132534	-9.452452E-09
E	-0.994202	3.18602E-08
F	-1163.336	-1174.135
H	-1120.894	-1120.894

A.2 NASA Polynomials

The NASA 7-coefficient polynomials for thermophysical properties of gas-phase species are formulated as follows [40]:

$$\begin{aligned} c_p\,[\text{J/(kg.K)}] &= R_g(A_1 + A_2T + A_3T^2 + A_4T^3 + A_5T^4) \\ h\,[\text{J/kg}] &= R_gT\left(A_1 + \frac{A_2T}{2} + \frac{A_3T^2}{3} + \frac{A_4T^3}{4} + \frac{A_5T^4}{5} + \frac{A_6}{T}\right) \end{aligned}$$

where T is the temperature in K, c_p is the gravimetric heat capacity at constant pressure, h is the gravimetric enthalpy, and R_g is the individual gas constant. The constants for the different species and the temperature ranges are shown in Tables A.4 to A.5 for the low and high temperature ranges.

Table A.4: NASA 7-coefficients polynomials for oxygen (O_2).

Range [K]	200-1000	1000-3500
A_1	3.78245636	3.28253784
A_2	-2.99673416E-03	1.48308754E-03
A_3	9.84730201E-06	-7.57966669E-07
A_4	-9.68129509E-09	2.09470555E-10
A_5	3.24372837E-12	-2.16717794E-14
A_6	-1.063943560E03	-1.08845772E03
A_7	3.65767573	5.45323129

Table A.5: NASA 7-coefficients polynomials for nitrogen (N_2).

Range [K]	300-1000	1000-5000
A_1	3.29868	2.92664
A_2	1.40824E-02	1.48798E-02
A_3	-3.96322E-06	-5.68476E-07
A_4	5.64152E-09	1.0097E-10
A_5	-2.44485E-12	-6.75335E-15
A_6	-1020.9	-922.798
A_7	3.95037	5.98053

Table A.6: NASA 4-coefficients polynomials for oxygen (O_2).

Range [K]	300-1000	1000-5000
A_1	0.77238828	0.90875998
A_2	6.9293259	289.86028
A_3	-5900.8518	-79180.433
A_4	1.2202965	0.068622859

Table A.7: NASA 4-coefficients polynomials for nitrogen (N_2).

Range [K]	300-1000	1000-5000
A_1	0.85372829	0.88506520
A_2	105.18665	134.69656
A_3	-12299.753	-11386.420
A_4	0.48299104	0.2361008

The NASA 4-coefficients correlation for transport properties of gas-phase species is formulated as follows:

$$k\,[\text{W/(m.K)}] = 1 \text{ x } 10^{-04}\left[\exp\left(A_1 \ln T + \frac{A_2}{T} + \frac{A_3}{T^2} + A_4\right)\right]$$

where T is the temperature in K, and k is the thermal conductivity. The constants for the different species and the temperature ranges are shown in Tables A.6 to A.7 for the low and high temperature ranges.

A.3 Diffusion Coefficient Empirical Parameters

The Fuller-Schettler-Giddins semi-empirical correlation is used to approximate the binary diffusion coefficient [49]:

$$D\,[\text{m}^2/\text{s}] = \frac{10^{-7} T^{1.75} \left[\frac{W_{\text{inert}} + W_{\text{O}_2}}{W_{\text{inert}} W_{\text{O}_2}}\right]^{1/2}}{\frac{p}{101325}\left[\left(\sum v\right)_{\text{O}_2}^{1/3} + \left(\sum v\right)_{\text{inert}}^{1/3}\right]^2}. \tag{A.1}$$

Table A.8: Empirical parameters $(\sum v)_i$ for the Fuller-Schettler-Giddins diffusion transport semi-empirical correlation.

Species	$(\sum v)$
O_2	16.6
N_2	17.9

where T is temperature in Kelvins, W_{inert} and W_{O_2} are molar weights of the inert gas and oxygen respectively in kg/kmol, p is pressure in Pa, and $(\sum v)_i$ are empirical parameters for the species provided in Table A.8.

Appendix B

Accommodation Coefficients

B.1 Thermal Accommodation Coefficient

The thermal accommodation coefficient α_{T} is a key parameter which governs the quantitative value of the ignition temperature of iron particles in the transition and free-molecular regimes. As stated in section 3.2.1, it has a strong dependence on the surface properties of the solid. There is large uncertainty in the data reported for the thermal accommodation coefficient of iron surfaces. Mohan et al. [17] report the thermal accommodation of metal surfaces should be within the range 0.50 to 0.90. Literature for different iron-gas pairs reports α_{T} scattered between 0.03 and 0.64 [50–53]. This high uncertainty makes difficult selecting a value of the thermal accommodation coefficient for computational studies.

Song & Yovanovich [33] proposed a semi-empirical correlation to characterize the thermal accommodation coefficient as a function of surface temperature and molar weight of the gas and surface. The parameters selected for the correlation rely on classical thermal accommodation theory and accounts for real surface effects such as gas adsorption on the solid surface. The proposed correlation agreed with available experimental data at the time to within 25%, which coincided with the scatter of the data. As the correlation permits a straightforward estimation of the energy accommodation coefficient for any solid-gas pair, it is retained in the current work. Table B.1 compares the

Table B.1: Comparison of thermal accommodation coefficients predicted by the Song & Yovanovich correlation to molecular dynamics and experimental results from different references.

Gas-surface pair	Surface Temperature [K]	Correlation	Comparison
Fe-He	2500	0.15	0.11 [50]
Fe-Ar	2500	0.59	0.23 [50]
Fe-N_2	800-1650	0.55-0.64	0.08 [52]
Fe-Ar	800-1650	0.60-0.67	0.19 [52]
Fe-N_2	800-1650	0.55-0.64	0.08 [51]
Fe-Ar	800-1650	0.60-0.67	0.155 [51]
Fe-He	2500	0.15	0.08 [53]
Fe-Ne	2500	0.47	0.14 [53]
Fe-Ar	2500	0.59	0.17 [53]
Fe-He	750	0.23	0.095 [54]

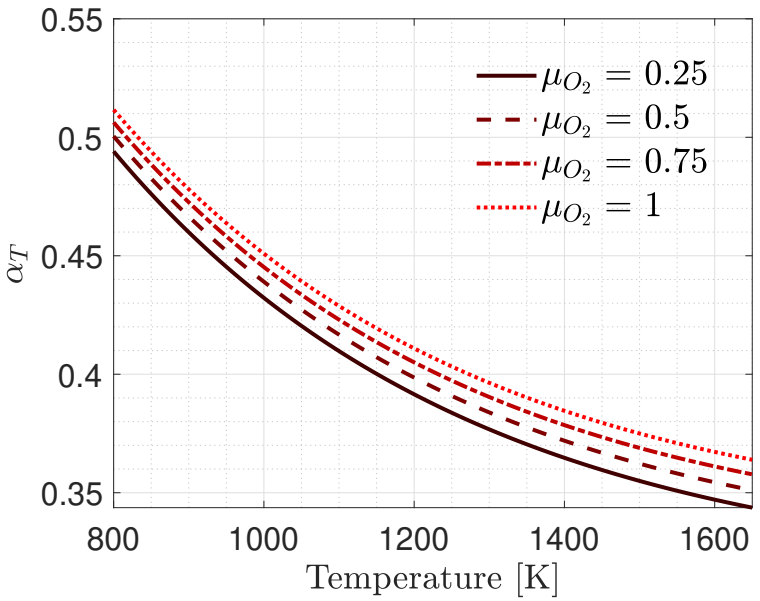

Figure B.1: Thermal accommmodation coefficient as a function of temperature for a Fe_2O_3-(O_2-N_2) system as predicted by the Song & Yovanovich semi-empirical correlation for different molar fractions of O_2 in the gas.

correlation to reported results in the literature for iron-gas systems. The estimations from the Song & Yovanovich [33] formula generally agree with the literature to within one order of magnitude. As well, α_T is plotted as a function of temperature in Figure B.1 for a Fe_2O_3-air system, at different oxidizer molar fractions. The values are approximately contained within the interval 0.35-0.51.

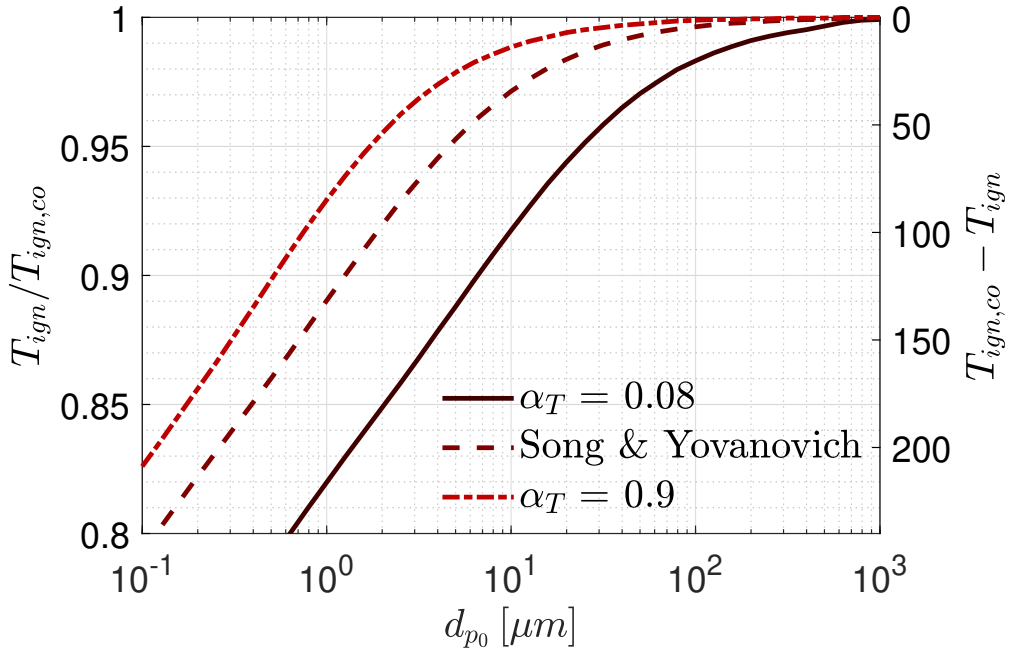

Figure B.2: Comparison of the ignition temperature obtained with different formulations for α_T to the continuum value for a constant $\delta_0 = 0.1$.

The lowest literature value of α_T reported in Table B.1 for a Fe-N_2 system is 0.08, while Mohan et al. [17] reported α_T could reach 0.90 for metals. A parametric study of the impact of α_T on the ignition temperature in this range is shown in Figure B.2. Decreasing α_T increases the minimum particle size at which transition transport effects become non-negligible. The results are computed with δ_0 = 0.10, as it leads to the highest threshold, as shown in Figure 5.7. For the lowest value of $\alpha_T = 0.08$, the 95% accuracy threshold is increased from $\approx$ 5 μm to 25 μm when compared to the Song & Yovanovich correlation results, while the 99% threshold is displaced from 40 μm to $\approx$ 200 μm. Recall the 95% threshold corresponds to a temperature differential of $\approx$ 50 K on ignition temperatures neighboring 1000 K, which cannot be resolved experimentally. The 95% threshold can therefore be considered as the continuum approximation limit. This threshold is still attained in the low tens of microns, while practical iron burner applications would use particles in the several tens or hundreds of microns. Hence, although there remains high uncertainty in quantifying α_T, the confidence interval of 0.08-0.90 overall does not impact the conclusion that transition transport effects can be neglected for large, practical size iron particles.

B.2 Mass Accommodation Coefficient

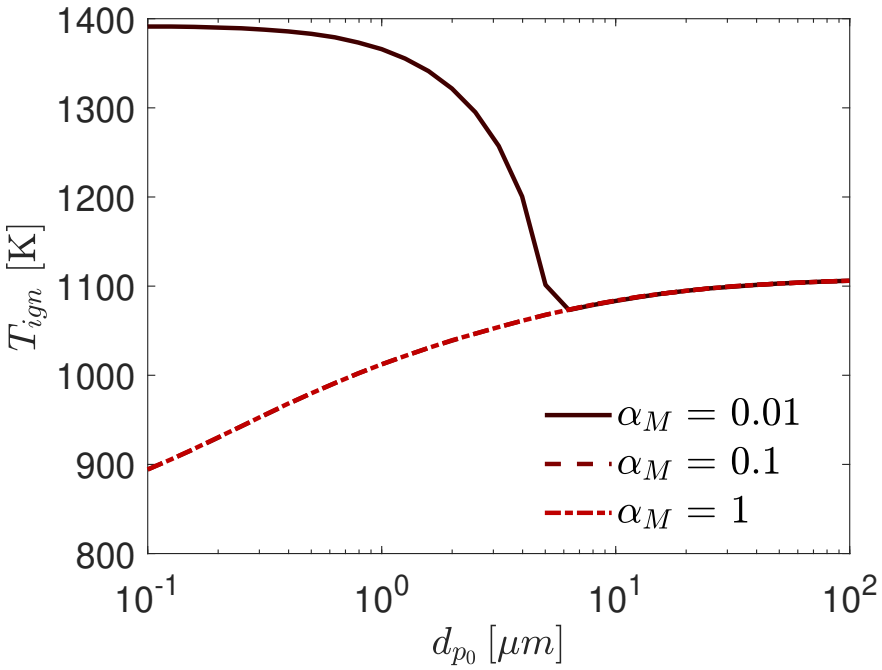

Figure B.3: Ignition temperature as a function of initial particle size with δ_0 = 0.01 for different values of the sticking coefficient.

The impact on the ignition temperature of varying the mass accommodation coefficient α_{M} over three orders of magnitude is shown in Figure B.3. The curves for α_{M} = 0.10 and α_{M} = 1 collapse into identical results. For α_{M} = 0.01, the ignition temperature initially decreases as the particle size is being decreased with a constant value of $\delta_0 = 0.01$, as expected. It follows the same curves as α_{M} = 0.10 and α_{M} = 1. However, it sharply increases as the particle size is decreased below $\approx$ 6.30 μm, and it eventually plateaus. This behavior suggests that the mass transport process governs the ignition behavior of very fine particles, as the delivery rate of oxidizer to the particle surface becomes small compared to the kinetic rates of the particle. The small particles burn fully in the diffusion-controlled regime at the ignition point, and the ignition becomes independent on the transition between the kinetic- and diffusive- limited regimes.

Simmons & Dwyer [30] performed a semi-empirical fit of the sticking coefficient as a function of oxygen exposure at the particle surface for iron reacting at an ambient pressure of 10^{-6} torr and at room temperature ($\approx$ 298 K). The lowest sticking coefficient they reported across the range studied is 0.20. Although the behavior observed in Figure B.3 for very small α_{M} is intriguing, this effect is observed only for exaggeratedly small values of α_{M}. In the current work, a value of $\alpha_{\mathrm{M}} = 0.10$ is retained for the analysis, and the ignition behavior is unaffected for values of α_{M} ranging between 0.10 and 1.

Appendix C

Mathematical Solution of the Implicit Boundary Sphere Method

The full formulation for the boundary sphere method requires solving an implicit system of three equations, three unknowns. The system can be solved using appropriate nonlinear numerical solvers for systems of equations. However, such an approach has shown to yield significant computing times and medium to low accuracy. Instead, the mathematical formulation outlined in the current appendix is implemented to solve the system of equations.

The approach aims to formulate all the unknowns as a function of T_θ only, to reduce the system of equations to a uni-variate problem. It can then be solved using a simple uni-variate root finding algorithm, such as the bisection algorithm. The system of Equations as described in Section 4.5 is:

$$\alpha_{\mathrm{T}}\pi r_{\mathrm{p}}^2\frac{p\bar{c}_\theta}{2}\left(\frac{\gamma_{\mathrm{p}}^*+1}{\gamma_{\mathrm{p}}^*-1}\right)\left(\frac{T_{\mathrm{p}}}{T_\theta}-1\right) = 4\pi(r_{\mathrm{p}}+\theta)k_{\mathrm{g},\theta}^*(T_\theta-T_{\mathrm{g}}) \quad \text{(C.1)}$$

$$\dot{m}_{\mathrm{O_2}} = \alpha_{\mathrm{M}}\pi r_{\mathrm{p}}^2(C_{\mathrm{O_2},\theta}\,\bar{c}_\theta - C_{\mathrm{O_2,p}}\,\bar{c}_p) \quad \text{(C.2)}$$

$$\dot{m}_{\mathrm{O_2}} = 4\pi(r_{\mathrm{p}}+\theta)D_\theta^*(C_{\mathrm{O_2,g}}-C_{\mathrm{O_2},\theta}). \quad \text{(C.3)}$$

C.1 Solution in the Kinetic-Limited Regime

In the kinetic limit, the unknowns are $\{T_\theta, C_{\mathrm{O}_2,\theta}, C_{\mathrm{O}_2,\mathrm{p}}\}$. In Equation C.3, the diffusion coefficient is:

$$\begin{aligned} D_\theta^* &= \frac{10^{-7} T_\theta^{*7/4} \left[\frac{W_{\text{inert}}+W_{\mathrm{O}_2}}{W_{\text{inert}} W_{\mathrm{O}_2}}\right]^{1/2}}{\frac{p}{101325}\left[\left(\sum v\right)_{\mathrm{O}_2}^{1/3} + \left(\sum v\right)_{\text{inert}}^{1/3}\right]^2} \\ \text{Let } K_1 &= \frac{101325 \text{ x } 10^{-7}}{p\left[\left(\sum v\right)_{\mathrm{O}_2}^{1/3} + \left(\sum v\right)_{\text{inert}}^{1/3}\right]^2}\left(\frac{W_{\text{inert}}+W_{\mathrm{O}_2}}{W_{\text{inert}} W_{\mathrm{O}_2}}\right)^{1/2} \end{aligned}$$

It follows that:

$$D_\theta^* = K_1 T_\theta^{*7/4}. \tag{C.4}$$

Equation C.3 then yields:

$$\dot{m}_{\mathrm{O}_2} = 4\pi(r_\mathrm{p}+\theta) K_1 T_\theta^{*7/4} (C_{\mathrm{O}_2,\mathrm{g}} - C_{\mathrm{O}_2,\theta})$$

It follows that:

$$\boxed{C_{\mathrm{O}_2,\theta} = C_{\mathrm{O}_2,\mathrm{g}} - \frac{\dot{m}_{\mathrm{O}_2}}{4\pi(r_\mathrm{p}+\theta) K_1 T_\theta^{*7/4}}}$$

which is a function of T_θ only, since $T_\theta^* = (2/3)T_\theta + (1/3)T_\mathrm{g}$. Given $C_{\mathrm{O}_2,\theta}$, $C_{\text{inert},\theta}$ can be computed using:

$$C_{\text{inert},\theta} = \left(\frac{p}{k_\mathrm{B} T_\theta} - \frac{C_{\mathrm{O}_2,\theta}}{m_{\mathrm{O}_2}}\right) m_{\text{inert}} = C_{\text{inert},\theta}(C_{\mathrm{O}_2,\theta}(T_\theta)) \equiv C_{\text{inert},\theta}(T_\theta)$$

a function of T_θ only. As well:

$$\begin{aligned} \bar{c}_\theta &= \sqrt{\frac{8k_\mathrm{B}T_\theta}{\pi}}\sqrt{\frac{C_{\text{inert},\theta}+C_{\mathrm{O}_2,\theta}}{C_{\text{inert},\theta} m_{\text{inert}} + C_{\mathrm{O}_2,\theta} m_{\mathrm{O}_2}}} = \bar{c}_\theta(C_{\text{inert},\theta}(T_\theta), C_{\mathrm{O}_2,\theta}(T_\theta)) \equiv \bar{c}_\theta(T_\theta) \\ C_{\text{inert,p}} &= \left(\frac{p}{k_\mathrm{B} T_\mathrm{p}} - \frac{C_{\mathrm{O}_2,\mathrm{p}}}{m_{\mathrm{O}_2}}\right) m_{\text{inert}} = C_{\text{inert,p}}(C_{\mathrm{O}_2,\mathrm{p}}) \\ \bar{c}_\mathrm{p} &= \sqrt{\frac{8k_\mathrm{B}T_\mathrm{p}}{\pi}}\sqrt{\frac{C_{\text{inert,p}}+C_{\mathrm{O}_2,\mathrm{p}}}{C_{\text{inert,p}} m_{\text{inert}} + C_{\mathrm{O}_2,\mathrm{p}} m_{\mathrm{O}_2}}} = \bar{c}_\mathrm{p}(C_{\text{inert,p}}(C_{\mathrm{O}_2,\mathrm{p}}), C_{\mathrm{O}_2,\mathrm{p}}) \equiv \bar{c}_\mathrm{p}(C_{\mathrm{O}_2,\mathrm{p}}) \end{aligned}$$

Given these relations, Equation C.2 can be re-written as:

$$\boxed{0 = C_{\mathrm{O_2},\theta}(T_\theta)\bar{c}_\theta(T_\theta) - C_{\mathrm{O_2,p}}\bar{c}_{\mathrm{p}}(C_{\mathrm{O_2,p}}) - \frac{\dot{m}_{\mathrm{O_2}}}{\alpha_{\mathrm{M}}\pi r_{\mathrm{p}}^2}}$$

a function of $C_{\mathrm{O_2,p}}$ and T_θ only. Given a value of T_θ, this equation can be solved numerically with a bisection algorithm for $C_{\mathrm{O_2,p}}$.

These formulations for $C_{\mathrm{O_2},\theta}$ and $C_{\mathrm{O_2,p}}$ are substituted in Equation C.1, allowing to express $\bar{c}_\theta$, γ_{p}^*, and $k_{\mathrm{g},\theta}^*$ as functions of T_θ only. The system of three equations, three unknowns is therefore reduced to a single equation with one unknown. An iterative root-finding algorithm can readily be applied to find the solution T_θ that satisfies Equation C.1. The overall procedure then consists on performing univariate rootfinding on a function of T_θ, while inside the function of T_θ, rootfinding for $C_{\mathrm{O_2,p}}$ is performed.

C.2 Solution in the Diffusion-Limited Regime

In the diffusive-limited regime, $C_{\mathrm{O_2,p}} = 0$, and the unknowns are $\{T_\theta,\, C_{\mathrm{O_2},\theta},\, \dot{m}_{\mathrm{O_2}}\}$. Equation C.4 is re-used to express the mass diffusion coefficient. Then, Equations C.2 and C.3 can be equated to yield:

$$\alpha_{\mathrm{M}}\pi r_{\mathrm{p}}^2 C_{\mathrm{O_2},\theta}\bar{c}_\theta = 4\pi(r_{\mathrm{p}}+\theta)K_1 T_\theta^{*7/4}(C_{\mathrm{O_2,g}} - C_{\mathrm{O_2},\theta}).$$

Given the relations:

$$\begin{aligned} C_{\mathrm{inert},\theta} &= \left(\frac{p}{k_{\mathrm{B}}T_\theta} - \frac{C_{\mathrm{O_2},\theta}}{m_{\mathrm{O_2}}}\right) m_{\mathrm{inert}} = C_{\mathrm{inert},\theta}(C_{\mathrm{O_2},\theta}) \\ \bar{c}_\theta &= \sqrt{\frac{8k_{\mathrm{B}}T_\theta}{\pi}}\sqrt{\frac{C_{\mathrm{inert},\theta} + C_{\mathrm{O_2},\theta}}{C_{\mathrm{inert},\theta}m_{\mathrm{inert}} + C_{\mathrm{O_2},\theta}m_{\mathrm{O_2}}}} = \bar{c}_\theta(C_{\mathrm{inert},\theta}(C_{\mathrm{O_2},\theta}), C_{\mathrm{O_2},\theta}, T_\theta) \equiv \bar{c}_\theta(C_{\mathrm{O_2},\theta}, T_\theta) \end{aligned}$$

this can be re-written as:

$$\boxed{0 = 4(r_{\mathrm{p}}+\theta)K_1 T_\theta^{*7/4}(C_{\mathrm{O_2,g}} - C_{\mathrm{O_2},\theta}) - \alpha_{\mathrm{M}} r_{\mathrm{p}}^2 C_{\mathrm{O_2},\theta}\bar{c}_\theta(C_{\mathrm{O_2},\theta}, T_\theta)}.$$

which is a function of T_θ and $C_{\mathrm{O}_2,\theta}$ only. Given a value of T_θ, this equation can be solved numerically for $C_{\mathrm{O}_2,\theta}$ with a bisection algorithm.

This formulation for $C_{\mathrm{O}_2,\theta}$ is substituted in Equation C.1, allowing to express $\bar{c}_\theta$, γ^*_{p}, and $k^*_{\mathrm{g},\theta}$ as functions of T_θ only. The system of three equations, three unknowns is therefore reduced to a single equation with one unknown. An iterative root-finding algorithm can readily be applied to find the solution T_θ that satisfies Equation C.1. The overall procedure then consists on performing univariate rootfinding on a function of T_θ, while inside the function of T_θ, rootfinding for $C_{\mathrm{O}_2,\theta}$ is performed. Then, $\dot{m}_{\mathrm{O}_2}$ can be resolved from either Equation C.2 or C.3.